



High-resolution correlations of strata within a sand-rich clinothem using grain fabric data, offshore New Jersey, USA

Grace I.E. Cosgrove*, David M. Hodgson*, Nigel P. Mountney*, and William D. McCaffrey*

School of Earth and Environment, University of Leeds, Leeds LS2 9JT, UK

■ ABSTRACT

Trajectories of successive clinofold rollovers are widely applied to predict patterns of spatio-temporal sand distribution. However, the detailed internal architecture of individual clinothems is rarely documented. Understanding the textural complexities of complete topset-foreset-bottomset clinothem sequences is a key factor in understanding how and when sediment is transferred basinward. This study used high-resolution, core-based analyses of 267 samples from three research boreholes from quasi-coeval topset, foreset, and bottomset deposits of a single Miocene intrashelf clinothem recovered during Integrated Ocean Drilling Program (IODP) Expedition 313, offshore New Jersey, USA. Topset deposits were subdivided into three sedimentary packages based on grain character and facies analysis, consisting of upper and lower river-dominated topset process-regime packages separated by a middle wave- and storm-dominated process-regime package. Temporal variability in topset process regime exerts a quantifiable effect on grain character across the complete depositional profile, which was used here to correlate topset deposits with time-equivalent sedimentary packages in foreset and bottomset positions. River-dominated sedimentary packages have higher sand-to-mud ratios; however, the grain character of river-dominated sedimentary packages is texturally less mature than that of wave- and storm-dominated deposits. Differences in grain character between packages dominated by different process regimes increase basinward. The novel use of quantitative grain-character data allows intraclinothem time lines to be established at a higher resolution than is possible using chronostratigraphic techniques. Additionally, stratigraphic changes in grain character were used to refine the placement of the basal sequence boundary. These results challenge the idea that clinofold trajectories and stacking patterns are sufficient to describe spatio-temporal sand-body evolution across successive clinothems.

■ INTRODUCTION

Clinothems form the principal architectural building blocks of many shelf-to-basin successions (e.g., Gilbert, 1885; Rich, 1951; Bates, 1953; Asquith, 1970; Mitchum et al., 1977; Pirmez et al., 1998; Adams and Schlager, 2000;

*E-mails: eegiec@leeds.ac.uk (Cosgrove); N.P.Mountney@leeds.ac.uk; D.Hodgson@leeds.ac.uk; W.D.McCaffrey@leeds.ac.uk

Bhattacharya, 2006; Patruno et al., 2015), and they are routinely subdivided geometrically into topset, foreset, and bottomset deposits. Clinothems form valuable archives of basin-margin evolution: The trajectories and geometries of consecutive clinofold rollovers and their resultant stacking patterns are widely applied to predict spatio-temporal sand distribution, in both the subsurface and in outcrop (e.g., Steel and Olsen, 2002; Johannessen and Steel, 2005; Helland-Hansen and Hampson, 2009; Jones et al., 2015; Koo et al., 2016; Chen et al., 2017; Pellegrini et al., 2017). Clinofold trajectory models have been developed to account for observed form in terms of the balance between the rates of sediment supply and the generation of accommodation space (e.g., Burgess and Hovius, 1998; Mellere et al., 2002; Steel and Olsen, 2002; Bullimore et al., 2005; Carvajal and Steel, 2006; Uroza and Steel, 2008; Helland-Hansen and Hampson, 2009; Ryan et al., 2009). The role of topset and shelf process regime in determining clinofold architecture and timing of sediment transfer has recently been emphasized as an important parameter to consider (e.g., Dixon et al., 2012a; Jones et al., 2015; Hodgson et al., 2018; Cosgrove et al., 2018).

Previous investigations of clinothem sequences have focused on understanding basin-scale relationships using multiple successive clinothems (e.g., Steel and Olsen, 2002; Johannessen and Steel, 2005; Helland-Hansen and Hampson, 2009; Dixon et al., 2012b; Koo et al., 2016; Chen et al., 2017; Pellegrini et al., 2017; Cosgrove et al., 2018). Understanding the internal architectural complexity of complete topset-foreset-bottomset clinothem sequences (including grain-size, grain shape and sand and mud content) is a key factor in understanding how and when sediment is transferred basinward, and in providing better constraint on the spatio-temporal sedimentary correlations of stratal units and their bounding surfaces. However, developing high-resolution intrasequence chronostratigraphic correlations is problematic, particularly in sand-rich successions. Stratigraphic changes in sedimentary facies can provide a means by which to correlate strata between wells, but this is fraught with uncertainty because of the transitional nature of facies change and the possibility for sediment bypass and nondeposition in one part of a clinothem that is time equivalent to deposits in other parts (Fig. 1). Biostratigraphic or chronostratigraphic constraints typically lack the necessary resolution to permit correlations of intrasequence surfaces. The limited understanding of intrasequence architecture is exacerbated by a paucity of sedimentological and stratigraphic documentation of individual clinothems with preserved coeval topset, foreset, and bottomset deposits (e.g., Carvajal and Steel, 2009; Carvajal et al., 2009; Wild et al., 2009; Grundvåg et al., 2014; Prélat et al., 2015; Koo et al., 2016).

To understand intraclinothem architecture at high resolution, both stratigraphically (up core) and longitudinally (dip parallel), and to determine linkages to topset process regime, this study utilized samples from three research boreholes recovered during Integrated Ocean Drilling Program (IODP) Expedition 313, offshore New Jersey, USA (Fig. 2). The cored intervals targeted topset, foreset, and bottomset deposits of a single Miocene clinothem sequence (m5.4; Fig. 3) using integrated analysis of grain character (size and shape; cf. Fildani et al., 2018) and core-based interpretation of sedimentary textures and structures. The aim of this study was to highlight how quantitative grain-character data can be used to better understand the cause(s) of intrasequence textural complexities. Specific research objectives were as follows: (1) to understand how topset process-regime signals (including depositional architecture and grain character) are propagated downdip into foreset and bottomset deposits; (2) to illustrate how topset process-regime variability impacts sediment texture down the complete two-dimensional (2-D), dip-parallel depositional profile; (3) to demonstrate the use of grain character to correlate intraclinothem, time-equivalent surfaces; and (4) to discuss how high-resolution grain-character data can be used as an additional tool to refine the placement of sequence boundaries.

Geological Setting

The Miocene United States (U.S.) middle Atlantic margin, spanning the shelf region offshore New Jersey, Delaware, and Maryland, is a siliciclastic-dominated prograding passive margin. This region has been tectonically quiescent since the opening of the Atlantic Ocean in the mid-Jurassic (Watts and Steckler, 1979). Therefore, the Mid-Atlantic margin offers a valuable natural laboratory in which to study mixed-energy coastal system successions in a tectonically stable setting (Katz et al., 2013). Furthermore, the succession preserves detailed microfossil and strontium isotope records, which provide good chronostratigraphic age control (Browning et al., 2013).

Rifting commenced during the Late Triassic (ca. 230 Ma; Sheridan and Grow, 1988; Withjack et al., 1998), with seafloor spreading active from the Middle Jurassic (ca. 165 Ma). The Jurassic section, in the region of the Baltimore Canyon Trough (Fig. 2), is mainly composed of limestones of shallow-water origin (8–12 km thick). The margin was fringed by a barrier reef complex until the mid-Cretaceous (Poag, 1985). During the Cenozoic, the tectonic history was dominated by simple thermal subsidence, sediment loading, and crustal flexure (Watts and Steckler, 1979; Reynolds et al., 1991). The Late Cretaceous to Paleogene interval was marked by generally low rates ($\sim 5000 \text{ km}^3 \text{ m.y.}^{-1}$; shelf width $>150 \text{ km}$) of siliciclastic and carbonate accumulation (Poag, 1985). Global and regional cooling resulted in a significant switch from carbonate ramp deposition to starved siliciclastic deposition during the late middle Eocene in onshore regions to earliest Oligocene further offshore on the slope (Miller and Snyder, 1997). The late Oligocene to Miocene interval was characterized by a dramatic increase in sedimentation rates (Poag, 1985; Miller and Snyder, 1997), the causes of which are poorly constrained, although some authors

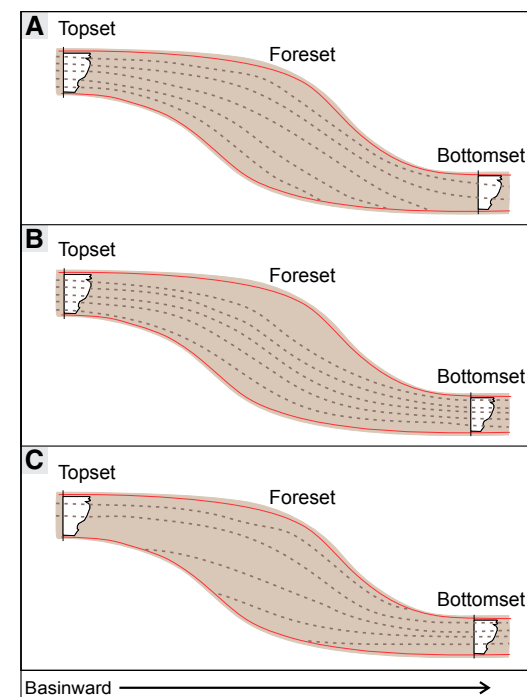


Figure 1. Schematic diagram of a clinothem sequence, with different internal correlations: (A) strongly progradational clinothem in which topset deposits are largely older than bottomset deposits; (B) aggradational clinothem in which topset deposits are the same relative age as bottomset deposits; (C) clinothem with strong early bypass, resulting in topset deposits that are largely younger than bottomset deposits. Sequence boundaries are shown in red. Dashed brown lines represent chronostratigraphic time lines from shallow- to deep-marine positions, illustrating permutations in intrasequence architecture.

have suggested it was the result of tectonic activity in the hinterland (Poag and Sevon, 1989; Sugarman et al., 1993). The late Oligocene to Miocene increase in sedimentation rates resulted in the growth of a siliciclastic sedimentary prism, consisting of multiple clinothem sequences, which prograded over the low-gradient shelf. The clinothems accumulated in an intrashelf setting, forming a seaward-thickening shelf prism (Hodgson et al., 2018). Intrashelf clinothems, or subaqueous deltas, are situated seaward of the shoreline break and landward of the continental break and typically have reliefs of tens of meters (Helland-Hansen and Hampson, 2009; Henriksen et al., 2009; Patruno et al., 2015; Hodgson et al., 2018).

IODP Expedition 313 drilled three research boreholes (Sites M27, M28, and M29), positioned to target the topset, foreset, and bottomset deposits of the Miocene intrashelf clinothems. The clinothems are well imaged on a grid of

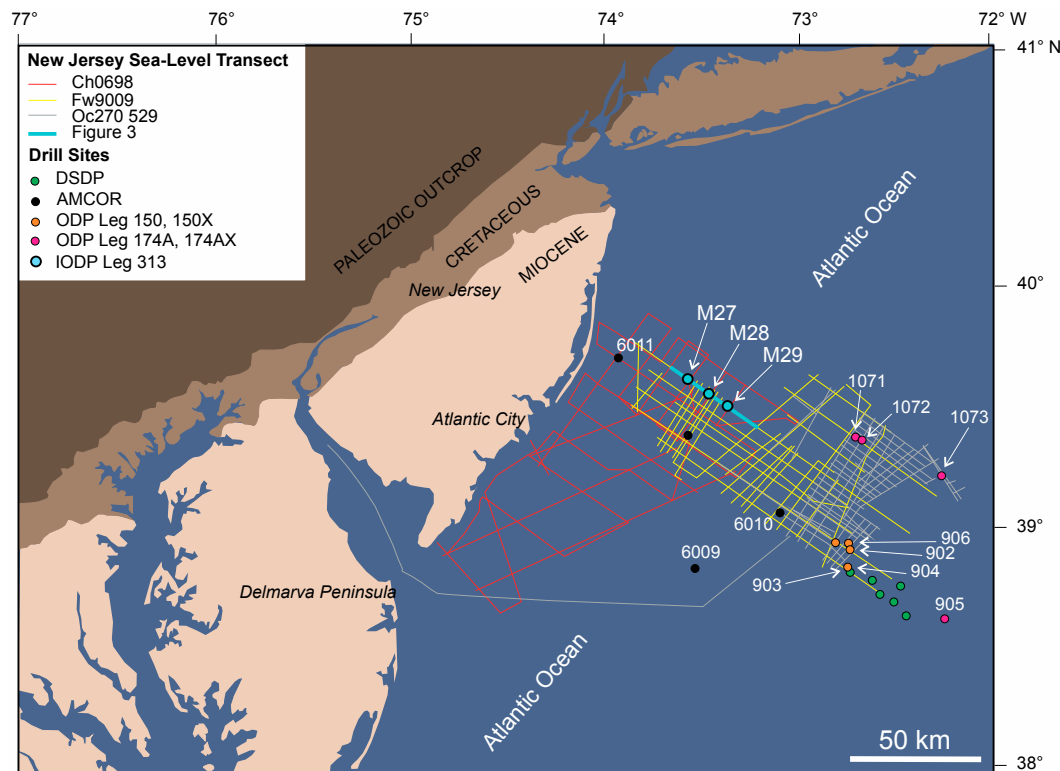


Figure 2. Location map of New Jersey sea-level transect, modified from Mountain et al., 2010. Study sites used in this paper (Integrated Ocean Drilling Program [IODP] Expedition 313 Sites M27, M28, and M29) are presented as blue circles. The seismic profiles indicated represent data acquired from three different cruises as part of the New Jersey sea-level transect (R/V *Ewing* cruise EW9009, R/V *Oceanus* cruise Oc270, and R/V *Cape Hatteras* cruise CH0698; Monteverde et al., 2008; Mountain et al., 2010; Miller et al., 2013a). The seismic line transecting the core sites M27–M29 (Oc270 529) is indicated in blue. This seismic transect is shown in Figure 3A. AMCOR—Atlantic Margin Coring Project; DSDP—Deep Sea Drilling Project; ODP—Ocean Drilling Program.

seismic profiles (Monteverde et al., 2008), which display the distinct sigmoidal geometries of the clinothem sequences (Fig. 3). Core sites M27, M28, and M29 were drilled in a transect along the trace of seismic line Oc270 529 (Fig. 2). Expedition 313 mapped 25 regional seismic surfaces of Oligocene to Miocene age, which correspond with changes in sedimentary facies in the associated core holes (Mountain et al., 2010). Integrated Sr-isotope stratigraphy and biostratigraphy (see Browning et al., 2013) was used to date sequences with a resolution of ± 0.25 –0.6 m.y. This study focused on sequence m5.4, which is of Miocene age (Mountain et al., 2010; Browning et al., 2013), and it is discussed in detail below.

Sequence m5.4

Sequence m5.4 was deposited over ~ 1.1 m.y. (17.7–16.6 Ma), with brief depositional hiatuses at its base and top (Browning et al., 2013). Integrated seismic data and stratigraphy suggest m5.4 is a composite sequence, composed of three higher-order depositional sequences (m5.4–1, m5.34, and m5.33; Miller

et al., 2013a) of ~ 100 k.y. duration; the higher-order sequences have been dated by regression of Sr-isotope data. Interpretations from previous studies of the stratigraphic depths of the composite sequence boundaries (m5.4 and m5.3) are illustrated in Figure 4, alongside interpretations of the higher-order sequence boundaries. For the purposes of this investigation, the placement of the m5.4 and m5.3 sequence boundaries will follow those presented in Miller et al. (2013a), who recognized sequence boundaries based on integrated core, seismic, and log data. The alternative published placements are described below.

Site M27

At site M27, the basal sequence boundary of m5.4 is placed at 295.01 meters composite depth (mcd) at an erosional surface (Miller et al., 2013a), which has been tied to synthetic seismogram data (Miller et al., 2013b). Originally, the m5.4 sequence boundary was placed at 271.23 mcd by Mountain et al. (2010). This surface was subsequently suggested by Miller et al. (2013a) to define the

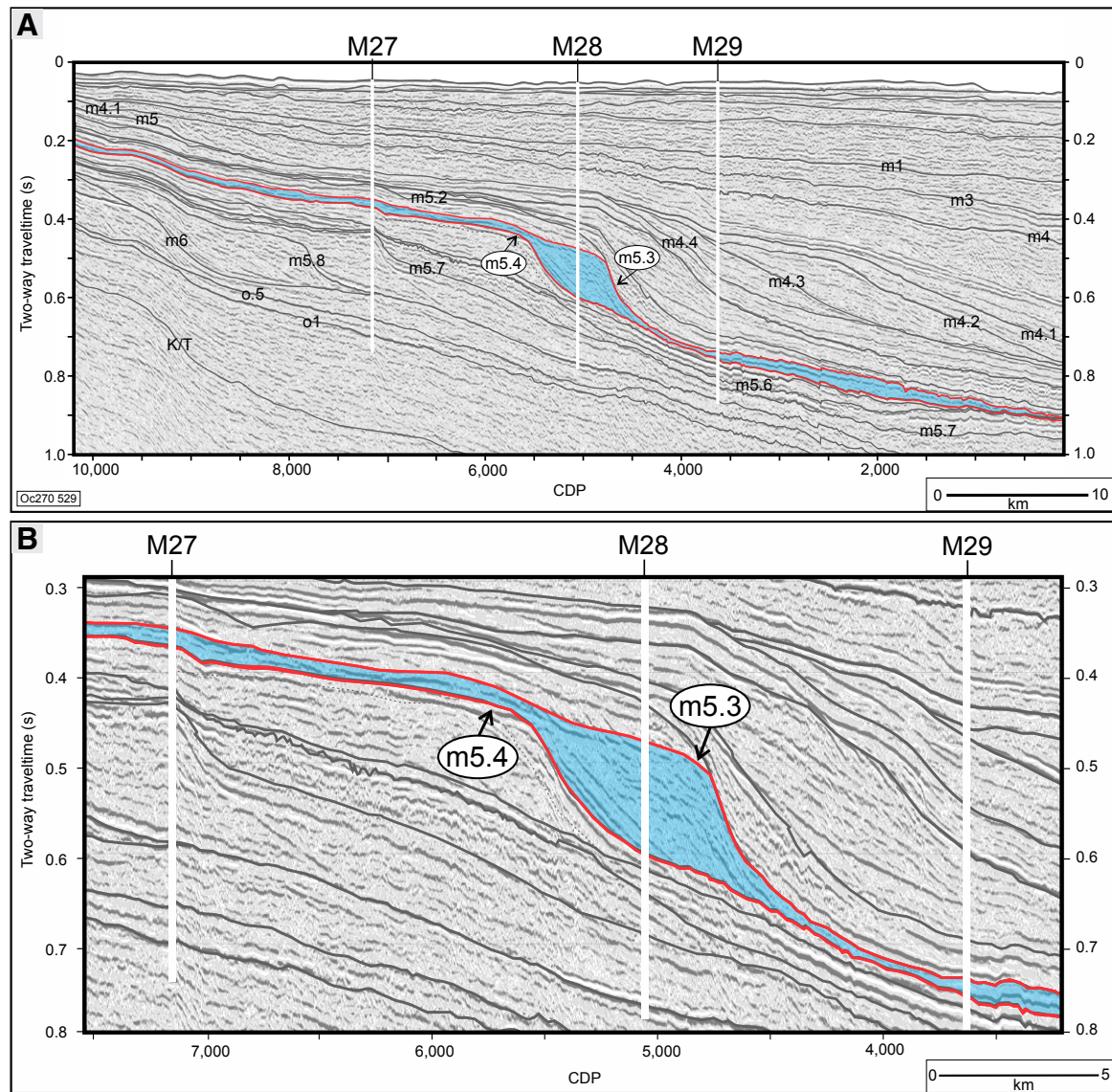


Figure 3. (A) Seismic line Oc270 529. Sequence boundaries relevant to this study are highlighted in red. Depositional sequence m5.4 is highlighted in blue. Depositional sequences are named in accordance with their basal reflector boundary; for example, sequence m5.4 lies on reflector m5.4. All seismic interpretations are from Monteverde et al. (2008), Mountain et al. (2010), and Browning et al. (2013). (B) Enlarged image of sequence m5.4 showing the intersection of cores M27–M29. K/T—Cretaceous-Tertiary; CDP—common depth point.

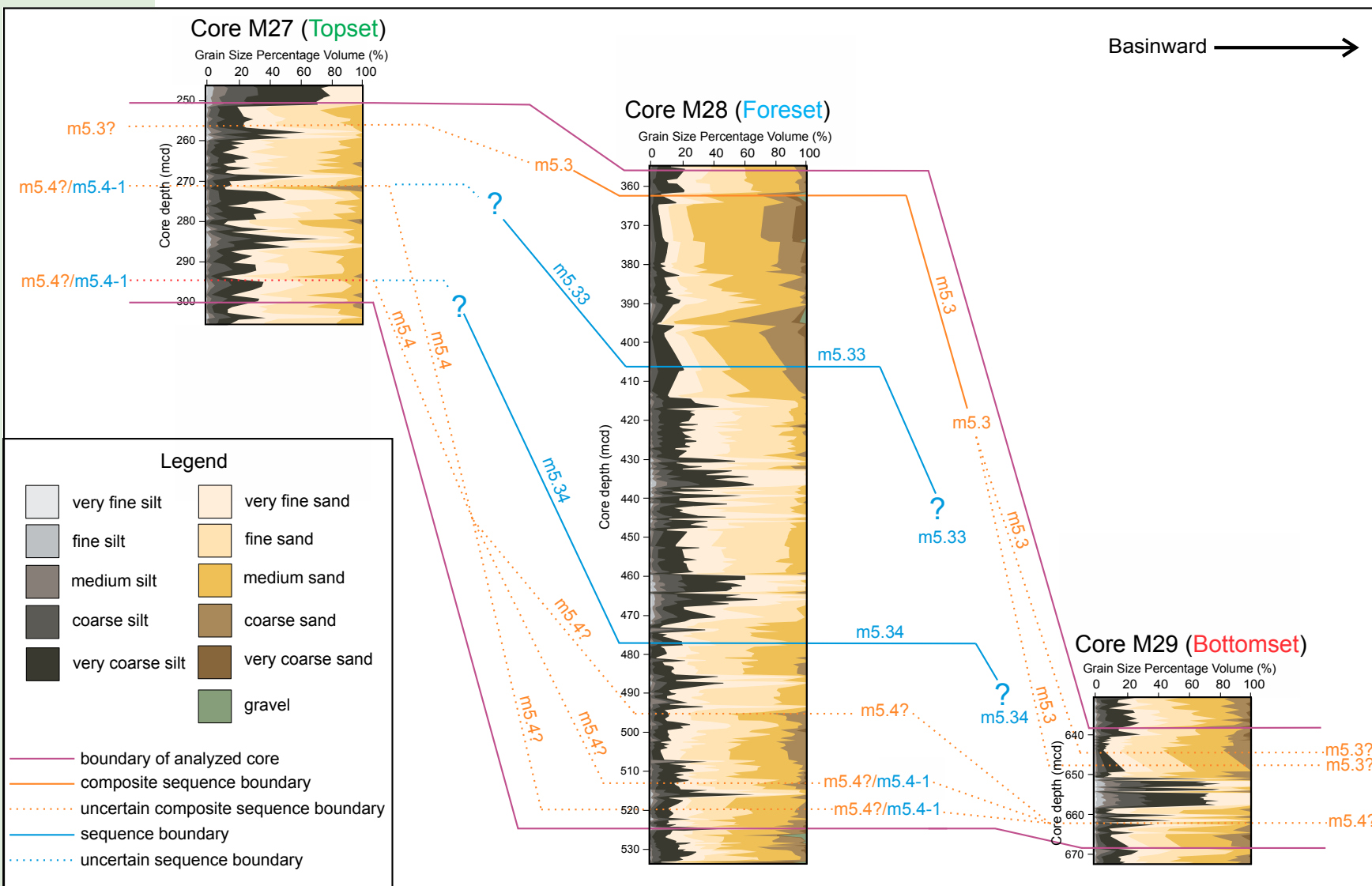


Figure 4. Correlation panel displaying various authors' composite sequence boundary (m5.3 and m5.4) and sequence boundary (m5.4-1, m5.34, and m5.33) interpretations (Mountain et al., 2010; Miller et al., 2013a, 2013b; Hodgson et al., 2018; Miller et al., 2018), where mcd is meters composite depth. The interpretations are overlain on new cumulative grain-size data plots from this study. Orange lines indicate composite sequence boundaries. Blue lines indicate intraclinothem sequence boundaries. Dashed lines are used to illustrate uncertainty, where the same (composite) sequence boundary has been interpreted at multiple core depths. The additional core sections described below and above the m5.4 and m5.3 sequence boundaries, respectively, are illustrated by the purple lines.

base of a higher-order sequence (m5.33). Sequence m5.4-1 is interpreted to have been cut out at Site M27 (Miller et al., 2013a); as such, m5.4 at Site M27 is a composite sequence consisting of the m5.34 (23.88 m thick; 295.01–271.13 mcd) and m5.33 (15.04 m thick; 271.23–256.19 mcd) sequences. Sr-isotope age estimates are 17.0–16.9 Ma and 16.6–16.5 Ma for sequences m5.34 and m5.33, respectively (Browning et al., 2013). The placement of the overlying m5.3 sequence boundary is equivocal and has been placed at 236.15 mcd (Mountain et al., 2010), 249.76 mcd (Miller et al., 2013b), and 256.19 mcd (Miller et al., 2013a). The 256.19 mcd sequence boundary placement was favored by Miller et al. (2013a) due to core expression, where a strongly bioturbated contact separates silt from an overlying coarse glauconite sand; this placement was also followed by Hodgson et al. (2018) and Proust et al. (2018).

Site M28

At Site M28, sequence m5.4 (151.30 m thick; 512.30–361.00 mcd) is bounded by two high-amplitude reflectors (m5.4 and m5.3) and has been recognized in previous studies (Monteverde et al., 2008; Mountain et al., 2010; Miller et al., 2013a, 2013b) based on termination styles of seismic reflectors at its base and top. Two alternative bases of sequence m5.4 were proposed by Mountain et al. (2010) at 495.20 mcd, where a thin sand bed overlies a clayey silt, and by Hodgson et al. (2018) at 519.70 mcd, where a sharp-based sand forms a fining-upward package of stratified sands with a deeply burrowed basal contact.

M5.4-1 is differentiated from the m5.4 sequence boundary but shares the same basal reflector. Sequence m5.4-1 (512.30–479.00 mcd) is ca. 17.7–17.6 Ma in age (Browning et al., 2013). M5.34 (479.00–405.00 mcd; 17.6–17.4 Ma; Browning et al., 2013) is interpreted to be a sequence boundary, as determined from seismic reflector termination patterns, including onlap, downlap, and the erosional truncation of the m5.4 sequence boundary (Miller et al., 2013b; Miller et al., 2018). M5.33 (405.00–361.00 mcd) is 16.7–16.6 Ma in age and is associated with a basal unconformity representing an ~0.7 m.y. hiatus (Browning et al., 2013). Terminations onto adjacent seismic profiles (onlap and erosional truncation) are associated with the M5.33 sequence boundary, as illustrated by a strike line taken at Site M28 (Miller et al., 2018).

Site M29

At Site M29 (19.18 m thick; 662.37–643.19 mcd; Miller et al., 2013b), Sr-isotope dating suggests sequence m5.4 has an age of 17.7–17.6 Ma; this age range corresponds to composite sequence m5.4-1 at Site M28, although this is poorly constrained (Browning et al., 2013). The basal m5.4 sequence boundary is placed at 662.37 mcd (Miller et al., 2013a), where a silty glauconite sand is overlain by a silt; the 662.37 mcd basal boundary is also supported by synthetic seismogram data (Miller et al., 2013b). Sequence m5.4 was originally

interpreted by Miller et al. (2013a) to pinch out after Site M28 and reappear at Site M29, as per the preceding description. However, an alternative interpretation was provided by Hodgson et al. (2018), in which sequence m5.4 is not present at Site M29; that interval in the core (spanning at least 662.37–649.16 mcd, with a coring gap from 649.16 to 644.28 mcd) is interpreted to represent the upper part of underlying sequence m5.45. At Site M29, the upper sequence boundary (m5.3) is placed at 643.19 mcd, where a sharp-based glauconite sand is deeply burrowed into an underlying silt; this sequence boundary is also associated with a large impedance contrast (Miller et al., 2013b). However, synthetic seismograms place the m5.3 seismic sequence boundary in a coring gap at 648.00 mcd (Miller et al., 2013b).

METHODS

This investigation employed two principal methodological approaches: (1) quantitative grain-character analysis and (2) paleoenvironmental interpretations of lithofacies, based on the visual core descriptions by the Expedition 313 sedimentologists and original core observations of lithology and sedimentary structures. According to the Miller et al. (2013a) scheme, the seismic sequence targeted in this investigation, sequence m5.4, spans the depths 295.00–256.19 mcd (38.81 m thick), 512.33–363.00 mcd (149.33 m thick), and 662.37–643.19 mcd (19.18 m thick) in cores M27, M28, and M29, respectively. An additional ~5 m of stratigraphy was also described from below the basal m5.4 sequence boundary (300.00–295.00 mcd and 667.00–662.37 mcd in core M27 and core M29, respectively). In core M28, an additional ~12 m of stratigraphy has been described (525.00–512.33 mcd), in order to include the alternative m5.4 sequence boundary proposed by Hodgson et al. (2018) at 519.70 mcd. Similarly, above the overlying sequence boundary for m5.3, an additional ~5 m of stratigraphy is also described (256.19–251.00 mcd, 361.00–356.00 mcd, and 643.19–638.00 mcd in cores M27, M28, and M29, respectively).

Facies Associations and Depositional Environments

Here, we present interpretations of lithofacies and depositional environments based on assemblages of sedimentary structures, sedimentary texture and composition, fossil content, and ichnofabric. These lithofacies show variability up core within sequence m5.4. Paleoenvironmental interpretations were based on the following: (1) a classic wave-dominated shoreline model (e.g., Reineck and Singh, 1972; McCubbin, 1982; Browning et al., 2006), which recognizes upper shoreface (0–5 m), lower shoreface (5–10 m), offshore transition (10–30 m), and offshore environments (>30 m); and (2) mixed river/wave delta facies models (e.g., Galloway, 1975; Bhattacharya and Walker, 1992). These have been summarized in Mountain et al. (2010) and Proust et al. (2018).

Grain-Character Analysis

The semilithified samples were subjected to a mechanical and chemical disaggregation process to remove organic matter and prepare them for grain-character analysis (see Cosgrove et al., 2018). Grain-character analysis was undertaken using a CamsizerXT (Retsch Technology), which is an optically based dynamic image analysis instrument capable of measuring grain sizes from 0.001 to 8 mm with an accuracy of ±1% (Moore et al., 2011). The grain-character analysis of the CamsizerXT yielded: (1) a grain-size distribution for each individual sample, with 105 logarithmically divided grain size classes spanning 0.001–8 mm, and (2) a fully quantified grain-shape value (sphericity and roundness) for each grain-size class within that grain-size distribution. The raw output data of the CamsizerXT were subsequently analyzed using GRADISTAT computer software (Blott and Pye, 2001). GRADISTAT allows rapid analysis of grain-size statistics from multiple sediment samples and provides values of the mean, mode, and sorting of the grain population, in addition to a grain-size cumulative frequency distribution for each sample. Grain-shape values were analyzed with Microsoft Excel software.

Within sequence m5.4, 63, 219, and 49 sediment samples were recovered from cores M27, M28, and M29, respectively. Due to the downdip change in clinothem thickness, the number of recovered samples varied between cores M27 and M29. Each core was subdivided into three sedimentary packages; this subdivision was based on the average grain-size distribution and corresponds to changes in sedimentary facies. The number of samples from each sedimentary package is displayed on the accompanying figures. Additionally, the exact core depth of each sample used in this investigation is provided in the Supplemental Information¹.

RESULTS

Core facies observations and descriptions are presented for sequence m5.4 at Sites M27, M28, and M29 in Tables 1–3, respectively. The tabulated lithofacies descriptions were supplemented by the sedimentary logs, which are presented in Figures 5A, 5B, and 5C for Sites M27, M28, and M29, respectively, and representative core photos (Fig. 6).

Topset Deposits (Core M27): Description

The core observations and descriptions are presented in Table 1.

Topset Deposits (Core M27): Interpretation

The topset deposits of sequence m5.4 form two broad facies associations: a coarser-grained facies (295.00–294 mcd and 273.00–256.19 mcd; Figs. 6A

and 6C) and an intervening finer-grained facies (~294–273.01 mcd; Fig. 6B). Within the coarse facies, the cross-lamination separated by undulating surfaces is interpreted as asymmetrical ripples formed by a unidirectional flow of fluvial origin. A fluvial source for the coarse facies is also supported by the presence of significant quantities of terrestrial material, including wood chunks and plant debris, concentrated within these stratigraphic intervals (e.g., Plink-Björklund and Steel, 2004; Rossi and Steel, 2016). The sand-rich nature of the coarse facies and the presence of gravel-sized detrital mineral grains (quartz and glauconite; Figs. 6A and 6C) suggest periods when river-flood events dominated, during which coarse sediment was rapidly deposited in a shoreface setting (e.g., Cosgrove et al., 2018).

Within the fine facies (Fig. 6B), the sand and silt interbeds are interpreted to be storm beds in a lower shoreface setting; convex-up laminations are interpreted to be hummocky cross-stratification. The presence of storm-beds, hummocky cross-stratification, and frequent shell-debris supports a wave- and storm-dominated process regime (e.g., Dott and Bourgeois, 1982; Harms et al., 1982).

Foreset Deposits (Core M28): Description

The core observations and descriptions are presented in Table 2.

Foreset Deposits (Core M28): Interpretation

The deposits of core M28 present either a coarse- or a fine-grained facies association with transitional changes observed between the facies. The foreset deposits of core M28 display a coarse-grained, glauconite-bearing facies (512.33–495 mcd and ~420.8–361.00; Figs. 6D and 6F) and an intervening fine-grained facies (~495–420.8 mcd; Fig. 6E).

The coarse-grained facies is predominantly expressed as medium-grained muddy sand that contains gravel-sized quartz and glauconite grains (Fig. 6D), and it represents deposition by mixed sediment gravity flows. The poorly sorted and unstratified nature of the coarse-grained facies suggests deposition by debris flows (Mulder and Alexander, 2001; Fig. 6F). Additionally, the presence of mud-chips and large volumes of detrital mineral grains (quartz and glauconite) suggests updip erosion and entrainment (Hodgson et al., 2018). Rare coarse-grained beds that display normal grading, and cross- and parallel-laminations, are interpreted to be the result of high-concentration turbidity currents (Mulder and Alexander, 2001). The abundant terrestrial debris and amount of mica suggest that fluvial processes at the shelf edge were responsible for the deposition of the coarse-grained facies. The dominant fluvial processes responsible for the deposition of the coarse-grained facies are suggested to be river-flood events that induced remobilization of shelf-edge deposits (cf. Normark and Piper, 1991; Zavala et al., 2006).

Within the finer-grained facies (Fig. 6E), the presence of both low-angle cross-laminations and convex-up laminations (hummocky cross-stratification)

Core M27 (Topset)					
SITE	CORE NUMBER	SECTION	TOP DEPTH	BOTTOM DEPTH	MCD
Boundary of analyzed zone					
27	88	1	46	47.8	250.22
27	88	1	116	117.2	250.56
27	88	2	26	27.2	281.73
27	88	2	105	106	292.21
27	88	1	46	41.8	283.21
27	88	2	105	111.8	293.21
27	88	2	26	21.8	284.21
27	88	2	105	111.8	294.21
27	88	2	120	121.2	295.21
m5.4 Sequence Boundary (Mulder et al., 2018)					
27	60	1	42	41.8	256.22
27	60	1	80	81.2	256.66
27	60	1	120	120.8	257.01
27	60	3	60	61.2	258.44
27	61	1	26	21.2	259.11
27	61	1	68	69.2	259.88
27	61	2	12	11.8	260.51
27	61	2	60	61.2	261.01
27	61	2	120	120.8	261.58
27	62	2	24	23.8	262.52
27	62	2	60	60.8	263.01
27	62	2	120	120.8	263.44
27	62	3	20	21.2	264.52
27	62	3	72	73.2	265.04
27	62	3	132	133.2	265.18
27	63	1	68	69.2	265.91
27	63	1	115	116.2	266.12
27	63	2	20	21.2	266.74
27	63	2	72	73.2	267.21
27	63	2	120	121.2	267.74
27	64	1	10	11.2	268.16
27	64	1	60	60.8	268.71
27	64	1	120	120.8	269.11
27	64	2	80	81.2	270.58
27	64	2	130	131.2	271.01
27	64	3	120	121.2	272.58
27	65	1	25	27.2	271.37
27	65	1	68	69.2	271.78
27	65	1	120	120.8	272.18
Sequence 3					
27	66	1	25	26.8	274.41
27	66	1	137	138.2	275.03
27	66	2	60	61.2	276.02
27	66	2	100	101.2	276.52
27	66	2	140	141.2	277.12
27	67	1	36	36.8	277.54
27	67	1	83	84.2	278.04
27	67	1	134	135.2	278.51
27	67	2	68	69.2	279.29
27	67	2	107	108.2	279.79
27	68	1	21	22.2	280.41
27	68	1	65	66.2	281.11
27	68	2	18	19.2	281.84

¹Supplemental Information. Data table showing the core depth of all samples used in this investigation for grain character analysis. Please visit <https://doi.org/10.1130/GES02046.S1> or access the full-text article on www.gsapubs.org to view the Supplemental Information.

indicates wave and storm reworking (e.g., Dott and Bourgeois, 1982; Harms et al., 1982). Additionally, the discrete sharp-based, normally graded sand beds interbedded with coarse-grained silt indicate episodic sediment flux associated with storm events (Reineck and Singh, 1972). The finer-grained facies are interpreted to represent deposition on a wave- and storm-dominated shelf. This sedimentary package can be tentatively associated with the finer-grained package found in the topset deposits of core M27.

Bottomset Deposits (Core M29): Description

The core observations and descriptions are presented in Table 3.

Bottomset Deposits (Core M29): Interpretation

The deposits of core M29 present either coarse- or fine-grained facies associations; however, interpretations of the exact stratigraphic segregation

of these facies are somewhat subjective because no abrupt facies changes are present. The bottomset deposits of core M29 display a coarse-grained, glauconite-bearing facies (662.37–658.50 mcd and ~651.6–643.19 mcd; Figs. 6G and 6I) and an intervening fine-grained facies (~658.5–651.6 mcd; Fig. 6H). The coarse-grained facies is typified by structureless glauconite-bearing sand interbedded with planar-laminated glauconite sand. The coarse-grained intervals are interpreted to represent rapid deposition of glauconitic sands from high-density turbidity currents and debris flows (Hodgson et al., 2018). The fine-grained facies is dominated by a structureless silt, predominantly representing deposition from suspension fallout, either from surface plumes or low-density turbidity currents.

Process Summary

Across the depositional profile, the fine-grained facies show a predominant wave and storm influence, recognized by: (1) abundant hummocky cross-stratification in the deposits of cores M27 and M28; (2) sandy-silt

TABLE 1. SUMMARY OF THE OBSERVED LITHOLOGY AND SEDIMENTARY TEXTURE OF THE CORE M27 DEPOSITS

Depth (mcd)		Thickness (m)	Lithology			Sedimentary structures	Glauconite/quartz	Terrestrial organic matter	Bioturbation index	Notes	Facies	Facies transition
Base	Top		Grain size	Sorting	Grading							
300*	295.01	~5	Clayey-silt	Average	Normal		Not present	Abundant and finely disseminated lignite	3/5	Clayey-silt containing abundant terrestrial organic matter. The upper bounding surface at 295.01 is an erosional surface demarcating m5.4 sequence boundary (Miller et al., 2013b).	N/A	Abrupt
295.01 [†]	294.25	~0.75	Coarse sand, fines upward to sandy-mud	Poor	Normal	Generally massive	Abundant angular glauconite and quartz grains (1–3 mm in diameter)	Abundant macroscopic plant fragments and lignite dispersed throughout	4	Poorly sorted coarse-grained glauconite sand. The stratigraphic interval fines upward to sandy-mud and contains abundant shell fragments and terrestrial organic matter.	Coarse grained	Transitional
294.24	~272.99	21.24	Coarse silt	Average	Normal	Low-angle laminations; convex-up laminations; planar laminations	Very rare gravel-sized glauconite found within convex-up laminations	Rare	2/3	Coarse-grained silt. The lower part of this stratigraphic interval is dominated by interbedded coarse-grained silts and sharp-based sands, associated with shell debris. The upper part of this unit is dominated by planar-laminated silt with rare fine-grained sand beds.	Fine grained	Abrupt
273.00	256.19 [§]	16.18	Medium to coarse sand	Poor	Normal	Asymmetrical ripples; undulating laminations	Rare rounded quartzite pebbles and subrounded glauconite granules (1–8 mm in diameter)	Macroscopic plant fragments throughout and a large wood chunk (~3 cm)	1	Poorly sorted coarse-grained glauconite sand. Coarsening-upward sand package with dispersed glauconite and quartz sand grains. The upper bounding surface of this unit is the m5.3 sequence boundary; the m5.3 sequence boundary is placed where an underlying silt is separated from a coarse-grained glauconite-sand by a bioturbated contact (Miller et al., 2013a).	Coarse grained	Abrupt
256.19	251*	~5	Silty sand	Good	Normal	Subhorizontal laminations	Localized medium-grained sand-sized glauconite grains	Finely disseminated organic matter	3	Laminated silty-sand with concentrated shell debris.	N/A	Abrupt

Note: mcd—meters composite depth.
 *Arbitrary point 5 m below m5.4 sequence boundary.
[†]m5.4 sequence boundary (Miller et al., 2013b).
[§]m5.3 sequence boundary (Miller et al., 2013a).
 *Arbitrary point 5 m above m5.3 sequence boundary.

TABLE 2. SUMMARY OF THE OBSERVED LITHOLOGY AND SEDIMENTARY TEXTURE OF THE CORE M28 DEPOSITS

Depth (mcd)		Thickness (m)	Lithology			Sedimentary structures	Glauconite/quartz	Terrestrial organic matter	Bioturbation index	Notes	Facies	Facies transition
Base	Top		Grain size	Sorting	Grading							
525*	519.7*	5.3	Silty-clay	Poor	Normal	Generally massive	Medium-grained sand– to gravel-sized (0.25–4 mm) quartz and glauconite grains. Glauconite forms between 1% and 25% of the total sediment volume.	Not present	4/5	Poorly sorted silty-clay containing abundant glauconite and quartz grains. The stratigraphic interval fines upwards and terminates at a bioturbated contact at 519.7 mcd (alternative m5.4 sequence boundary; Hodgson et al., 2018).	N/A	Transitional
519.7†	~517	2.7	Coarse sand	Poor	Normal	Generally massive	Abundant medium-grained sand– to gravel-sized glauconite (0.25–4 mm). Glauconite forms between 7% and 40% of the total sediment volume.	Not present	2/5 (highly variable)	Poorly sorted glauconite sand.	N/A	Abrupt
~517	512.33**	~4.67	Sandy-silt	Average	Normal	Parallel laminations	Not present	Finely disseminated organic matter is concentrated into ~2-mm-thick laminae.	4/5	Sandy-silt. The stratigraphic interval fines upwards and terminates at a bioturbated contact at 512.33 mcd (m5.4 sequence boundary; Miller et al., 2013a).	N/A	Abrupt
512.33	~495	~17.33	Fine to coarse sand	Poor	Normal	Parallel laminations; rip-up clasts (mud chips)	Local gravel- and pebble-sized (3–8 mm), subrounded to subangular quartz and glauconite grains.	Common throughout; found both dispersed and concentrated into ~2-mm-thick laminae. Rare larger wood chunks are found in association with glauconite and quartz grains.	4	Poorly sorted micaceous sand, containing localized glauconite- and quartz-rich sands.	Coarse grained	Transitional
~495	420.8	~74.2	Coarse silt	Average	Normal	Parallel laminations; low-angle cross-laminations; convex-up laminations; scours	Not present	Very finely disseminated organic matter is present.	2	Coarse-grained silt. The base of this stratigraphic interval is dominated by a fine-grained sand that fines upward to a coarse-grained silt. The sandy base is associated with a transitional facies change to the preceding coarse-grained stratigraphic interval. Within the coarse-grained silt, there are commonly occurring interbeds of coarse-grained silt and normally graded fine-grained sand (1–3 mm in thickness).	Fine grained	Transitional
420.8	361.00††	57.81	Medium to coarse sand	Poor	Normal	Rare parallel laminations at base	Local gravel- and pebble-sized (3–8 mm), subrounded quartz and glauconite grains.	Organic matter increases upwards associated with coarsening. The coarse sand is associated with larger wood chunks (up to ~4 mm in length).	1	Poorly sorted, medium- to coarse-grained glauconite sand. The unit coarsens upward from coarse-grained silt at the base to a coarse-grained sand. The silty base of this stratigraphic interval is associated with a transitional facies change to the preceding fine-grained stratigraphic interval. The expression of the m5.3 sequence boundary (361.00 mcd; Miller et al., 2013a; Miller et al., 2018) is subtle in core, but it is associated with major gamma-log changes (Miller et al., 2013a).	Coarse grained	Transitional
361.00§	356§§	5	Medium to coarse sand	Poor	Normal	Generally massive	Local medium-grained sand–sized (0.25–0.5 mm) glauconite grains. Glauconite forms between 1% and 3% of the total sediment volume.	Rare finely disseminated organic matter.	3/4	Poorly sorted medium- to coarse-grained glauconite sand. The stratigraphic interval shows an overall fining-upward trend.	N/A	Transitional

Note: mcd—meters composite depth.

*Arbitrary point 12 m below the m5.4 sequence boundary as presented in Miller et al. (2013a) and 5 m below the alternative m5.4 sequence boundary as presented in Hodgson et al. (2018).

†Alternative m5.4 sequence boundary (Hodgson et al., 2018).

‡m5.3 sequence boundary (Miller et al., 2013a; Miller et al., 2018).

§Alternative m5.4 sequence boundary (Hodgson et al., 2018).

¶m5.4 sequence boundary (Miller et al., 2013a).

††m5.3 sequence boundary (Miller et al., 2013a; Miller et al., 2018).

§§Arbitrary point 5 m above m5.3 sequence boundary.

TABLE 3. SUMMARY OF THE OBSERVED LITHOLOGY AND SEDIMENTARY TEXTURE OF THE CORE M29 DEPOSITS

Depth (mcd)		Thickness (m)	Lithology			Sedimentary structures	Glauconite/quartz	Terrestrial organic matter	Bioturbation index	Notes	Facies	Facies transition
Base	Top		Grain size	Sorting	Grading							
667*	662.37 [#]	4.63	Coarse-grained sand	Moderate	Normal	Generally massive	Abundant coarse-grained sand-sized (0.5–1 mm) quartz and glauconite grains. Quartz and glauconite forms between 20% and 70% of the total sediment volume.	Not present	1	Coarse-grained glauconite sand. This stratigraphic interval terminates at the m5.4 sequence boundary (662.37 mcd; Miller et al., 2013a), where glauconite sand is overlain by a silty-clay.	N/A	Abrupt
662.37 [†]	658.01	10.87	Coarse-grained sand	Poor	Normal	Generally massive; rare parallel laminae	Abundant coarse-grained sand- to gravel-sized (0.5–4 mm) quartz and glauconite grains. Locally, the glauconite content can reach up to ~70% of the total sediment volume, where glauconite is concentrated into ~2-cm-thick parallel laminae. Glauconite is also found concentrated in burrows.	Terrestrial organic matter is concentrated locally in laminae.	5	Coarse-grained glauconite and quartz sand.	Coarse grained	Transitional
658.01	651.6	6.41	Coarse-grained silt	Moderate	Normal	Structureless	Not present	Not present	3	Structureless coarse-grained silt. The base of the stratigraphic interval is a fine-grained sand, which fines upward to a coarse-grained silt. The sandy base of this interval is associated with a transitional facies change to the preceding coarse-grained stratigraphic interval.	Fine grained	Transitional
651.6	643.19 ^{**}	8.41	Medium-grained sand	Poor	Normal	Generally massive	Abundant fine-grained to coarse-grained sand-sized (0.125–1 mm) glauconite and quartz are present within a sandy matrix. Locally, the glauconite can form up to ~80% of the total sediment volume.	Finely disseminated organic matter is found concentrated locally.	0/4 (variable)	Structureless glauconite and quartz sand. The base of this stratigraphic interval has a silty matrix, which contains glauconite and quartz grains of medium-grained sand size (0.25–0.5 mm). The matrix coarsens upward throughout the stratigraphic interval. The relatively siltier base of this interval is associated with a transitional facies change between this stratigraphic interval and the preceding finer-grained stratigraphic interval. The bioturbation index varies according to glauconite content: where glauconite is >40% of the total sediment volume, the bioturbation index is 1–0; where glauconite is <40% of the total sediment volume, the bioturbation index is 4. The stratigraphic interval terminates at the m5.3 sequence boundary (643.19 mcd; Miller et al., 2013a), where an overlying glauconite sand is deeply burrowed into an underlying silt.	Coarse grained	Transitional
643.19 [§]	638 ^{††}	5.19	Silty-sand	Poor	Normal	Generally massive	Medium- and coarse-grained sand-sized (0.25–1 mm) glauconite grains are found within a sandy-silt matrix. Glauconite can form up to ~80% of the total sediment volume.	Not present	1/5 (variable)	Silty glauconite sand.	N/A	Abrupt

Note: mcd—meters composite depth.

*Arbitrary point 5 m below m5.4 sequence boundary (Miller et al., 2013a).

[†]m5.4 sequence boundary (Miller et al., 2013a).

[§]m5.3 sequence boundary (Miller et al., 2013a).

[#]m5.4 sequence boundary (Miller et al., 2013a).

^{**}m5.3 sequence boundary (Miller et al., 2013a).

^{††}Arbitrary point 5 m above the m5.3 sequence boundary (Miller et al., 2013a).

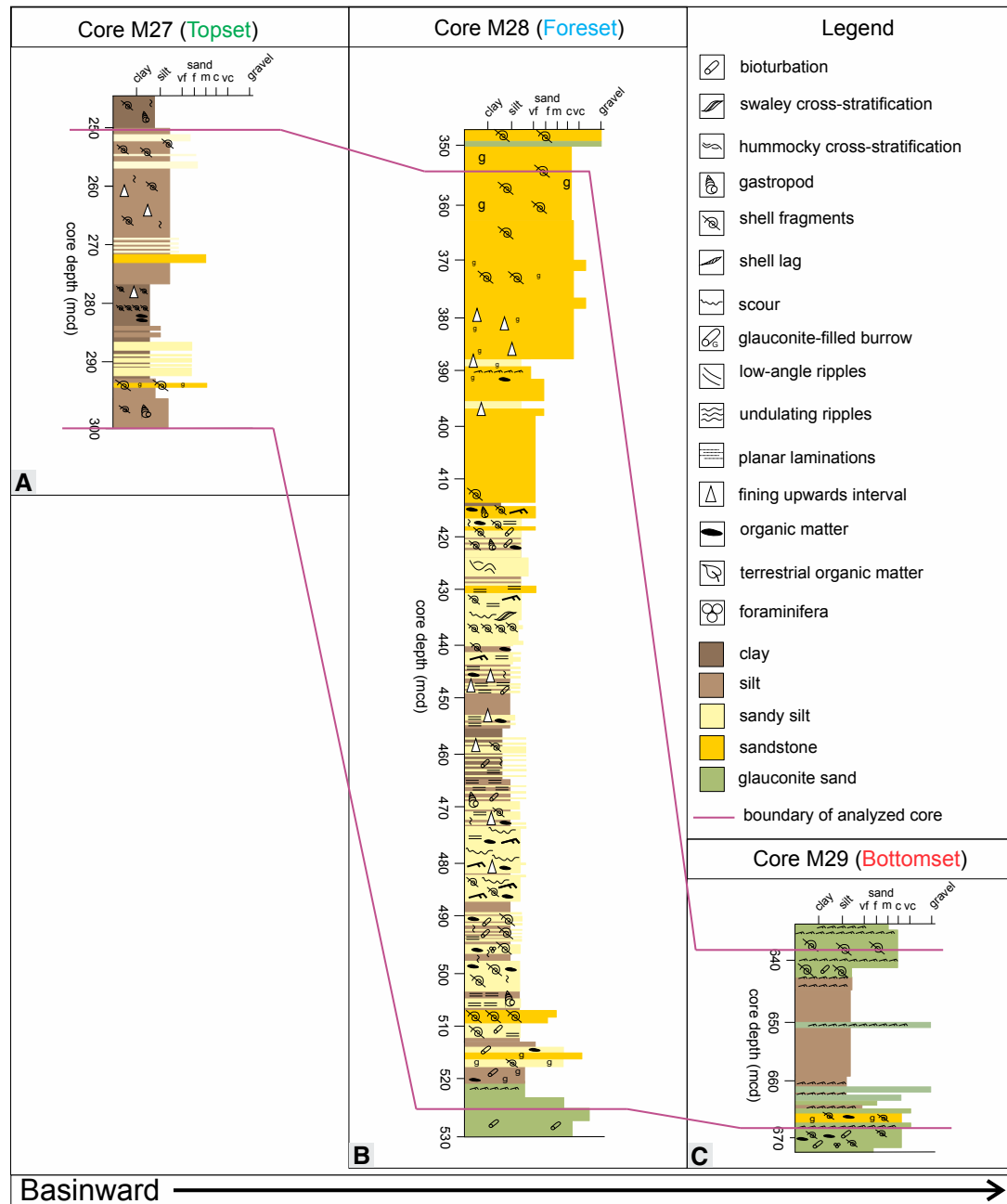


Figure 5. Simplified lithologic columns for Sites M27 (A), M28 (B) and M29 (C). Purple lines illustrate the boundaries of the core described in Tables 1–3; mcd—meters composite depth. Grain-size abbreviations: vf—very fine, f—fine, m—medium, c—coarse, vc—very coarse.

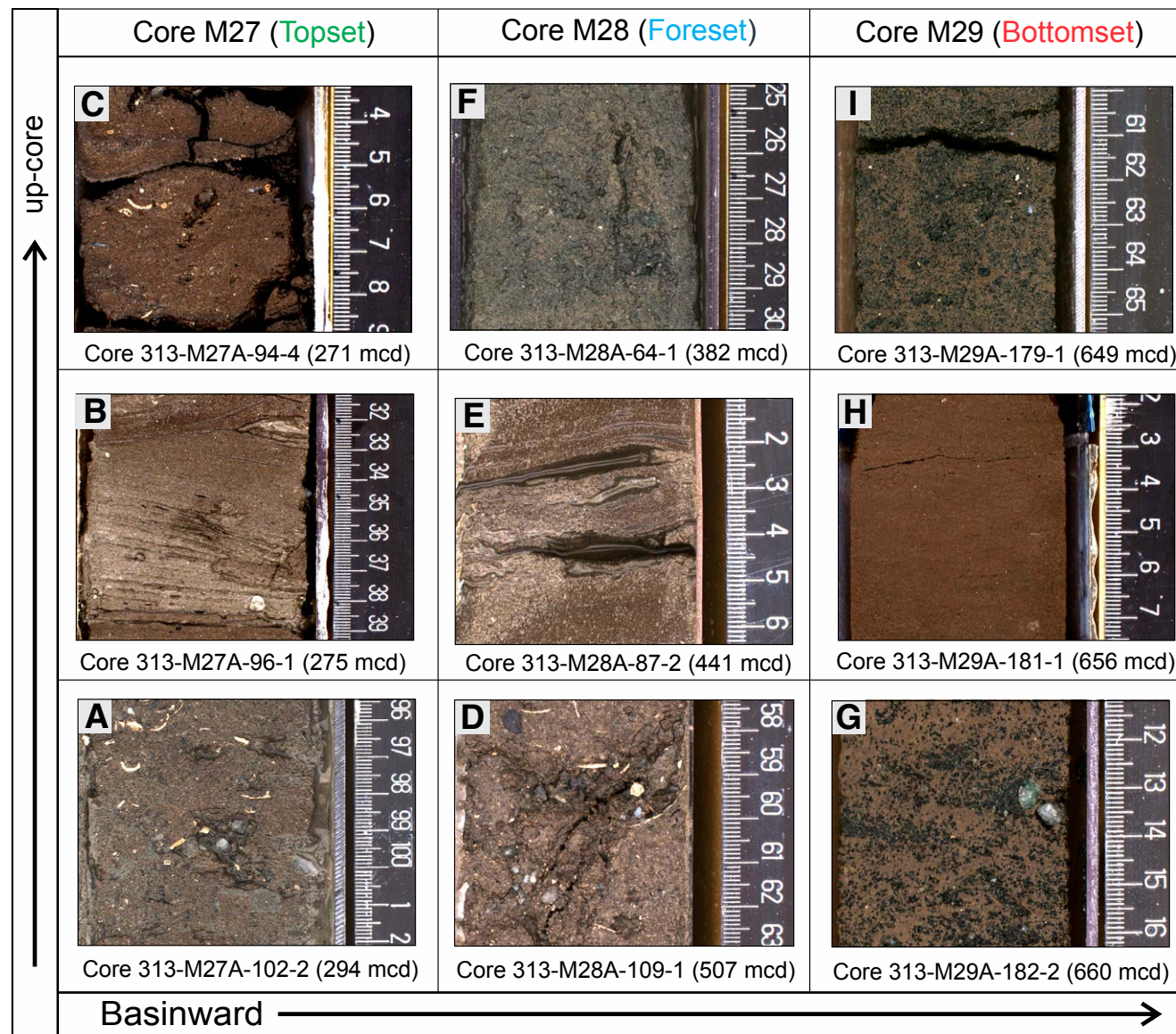


Figure 6. Representative core photographs: (A) coarse sand containing detrital quartz and glauconite grains and shell fragments; (B) hummocky cross-stratification; (C) fine sand containing detrital quartz and glauconite grains; (D) coarse sand containing detrital quartz and glauconite grains; (E) swaley cross-stratification; (F) structureless coarse glauconite sand; (G) silty-sand containing quartz and glauconite; (H) structureless silt; (I) structureless coarse sand. Numerical code associated with each core photo refers to the expedition number (e.g., 313), the core location (e.g., M29), and the core number (e.g., 181-1). The core depth is also shown (mcd—meters composite depth).

interbeds, representing episodic sediment flux associated with storm events; and (3) silt-dominated foreset and bottomset deposits, indicating an absence of direct fluvial sediment delivery. In contrast, the coarse-grained facies shows a predominant river influence, recognized by: (1) the strong terrestrial influence displayed by this facies (abundant plant and wood debris); (2) the grain-size variation (granule- and pebble-sized quartz and glauconite grains); (3) unidirectional current indicators (asymmetrical ripples); and (4) debritic and turbiditic deposits in foreset and bottomset deposits, interpreted to result from river-flooding events and hyperpycnal flows, respectively.

Grain Character

Grain-character data are presented for the topset, foreset, and bottomset deposits of sequence m5.4. The observed facies changes correspond with changes in grain-size distribution. The changes in grain-size distribution noted below were used to subdivide sequence m5.4 deposits into three subunits (a, b, and c) at each site.

Topset Deposits (M27)

The grain-size distribution of samples from 295.00–294.26 mcd displays two principal peaks at 0.057 mm (very coarse-grained silt) and 0.35 mm (medium-grained sand; Fig. 7A). In contrast, from 294.25 to 273.00 mcd, the grain-size distribution displays one broad peak spanning 0.098–0.21 mm (very fine- to medium-grained sand; Fig. 7B). From 272.99 to 256.19 mcd, the grain-size distribution displays two principal peaks at 0.063 mm (very fine-grained sand) and 0.27 mm (medium grained-sand; Fig. 7C). These changes in grain-size distribution define three sedimentary packages in the topset deposits (core M27) of sequence m5.4, informally referred to as M27a (295.00–294.26 mcd), M27b (294.25–273.00 mcd), and M27c (272.99.00–256.19 mcd; Fig. 8). Additional differences in grain character in sedimentary package M27b relative to sedimentary packages M27a and M27c include a finer mean grain size (Fig. 9A), a lower sand-to-mud ratio (M27b = 70:30 [Fig. 10B], M27a = 71:29 [Fig. 10A], M27c = 74:26 [Fig. 10C]), and a higher mean sphericity (Fig. 9A; Table 4).

Foreset Deposits (M28)

The grain-size distribution of samples from 512.33–495.00 mcd displays two principal peaks at 0.0625 mm (very fine sand) and 0.25 mm (medium sand; Fig. 7D). In contrast, from 494.99 to 415.00 mcd, the grain-size distribution of the samples displays one broad peak spanning 0.0682–0.193 mm (very fine- to fine-grained sand; Fig. 7E). From 414.99 to 63.00 mcd, the grain-size distribution comprises two principal peaks at 0.0625 mm (very fine-grained sand) and 0.297 mm (medium-grained sand; Fig. 7F). These changes in grain-size distribution were

used to define three sedimentary packages within the foreset deposits (core M28) of sequence m5.4, informally referred to as M28a (512.33–495.00 mcd), M28b (494.99–415.00 mcd), and M28c (414.99–363.00 mcd; Fig. 8). Additional differences in grain character of M28b compared to M28a and M28c include a finer mean grain size (Fig. 11A), a lower sand-to-mud ratio (M28b = 73:27 [Fig. 10E], M28a = 88:12 [Fig. 10D], M28c = 84:16 [Fig. 10F]), better sorting (Fig. 11B), and more spherical (Fig. 11C) and well-rounded (Fig. 11D) grains (Table 5).

Bottomset Deposits (M29)

The grain-size distribution of samples from 662.37–658.50 mcd displays two principal peaks at 0.0625 mm (very fine sand) and 0.273 mm (medium sand; Fig. 7G). In contrast, from 658.49 to 651.64 mcd, the grain-size distribution displays one sharp, asymmetric peak at 0.0682 mm (very fine sand; Fig. 7H). A bimodal distribution returns from 651.63 to 643.19 mcd, where the grain-size distribution displays two principal peaks at 0.0682 mm (very fine sand) and 0.297 mm (medium grained-sand; Fig. 7I). The changes in grain-size distributions were used to define three sedimentary packages in the bottomset deposits of core M29, informally referred to as M29a (662.37–658.50 mcd), M29b (658.49–651.64 mcd), and M29c (651.63–643.19 mcd; Fig. 8). Additional differences in grain character of sedimentary package M29b, relative to sedimentary packages M29a and M29c, include a finer mean grain size (Fig. 12A), a lower sand-to-mud ratio (M29b = 37:63 [Fig. 10H], M29a = 84:16 [Fig. 10G], M29c = 81:19 [Fig. 10I]) and more spherical and rounded grains (Figs. 12C and 12D; Table 6).

Correlations across Topset-Foreset-Bottomset Profiles

In lieu of higher-resolution biostratigraphic and chronostratigraphic age control, quantitative grain-character data were used here as a lithostratigraphic tool to objectively subdivide the stratigraphy, and to correlate genetically related sedimentary packages, from topset through foreset to bottomset deposits of seismic sequence m5.4 (Fig. 8). The sedimentary packages are separated by two intraclinothem surfaces, based on abrupt changes in grain-size distribution, informally referred to in this study as surfaces 2 and 3; an additional surface (surface 1) corresponds to the basal m5.4 composite sequence boundary. Surface 2 separates sedimentary packages M27–M29a and M27–M29b and occurs at 294.26, 495.00, and 658.50 mcd in cores M27, M28, and M29, respectively. Surface 3 separates sedimentary packages M27–M29b and M27–M29c and occurs at 272.99, 415.00, and 651.64 mcd in cores M27, M28, and M29, respectively (Fig. 8). The correlated sedimentary packages between the surfaces are M27–M29a and M27–M29c, which correspond to the coarse-grained facies and topset deposits that have bimodal grain-size distributions, and which are coincident with river-dominated facies, and sedimentary package M27–M29b, which has a unimodal grain-size distribution and corresponds to the fine-grained package in the topset deposits that are wave-dominated.

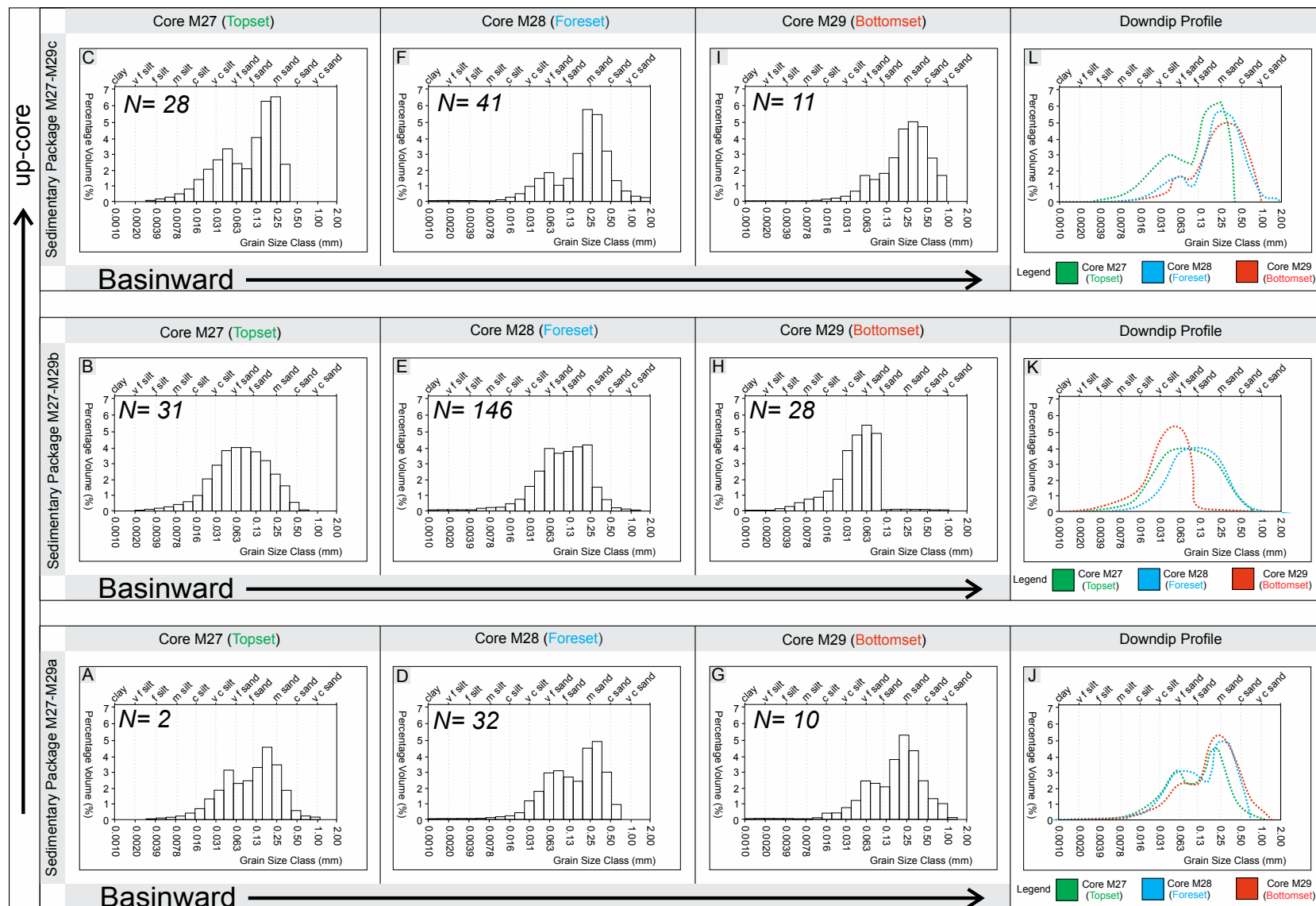


Figure 7. Average grain-size distribution profiles, which were used to subdivide m5.4 stratigraphy: (A) sedimentary package M27a; (B) sedimentary package M27b; (C) sedimentary package M27c; (D) sedimentary package M28a; (E) sedimentary package M28b; (F) sedimentary package M28c; (G) sedimentary package M29a; (H) sedimentary package M29b; (I) sedimentary package M29c; (J) average grain-size distribution profiles of core M27 (topset), core M28 (foreset), and core M29 (bottomset) deposits of sedimentary package M27–M29a; (K) average grain-size distribution profiles of core M27 (topset), core M28 (foreset), and core M29 (bottomset) deposits of sedimentary package M27–M29b; (L) average grain-size distribution profiles of core M27 (topset), core M28 (foreset), and core M29 (bottomset) deposits of sedimentary package M27–M29c. The y and x axes are percentage volume (%) and grain size (mm), respectively. Alongside the numerical grain-size classes, the descriptive grain-size classes are modified from Udden (1914) and Wentworth (1922). The number of samples used to produce each grain-size distribution profile is shown by $N = X$. Grain-size abbreviations: vf—very fine, f—fine, m—medium, c—coarse, vc—very coarse.

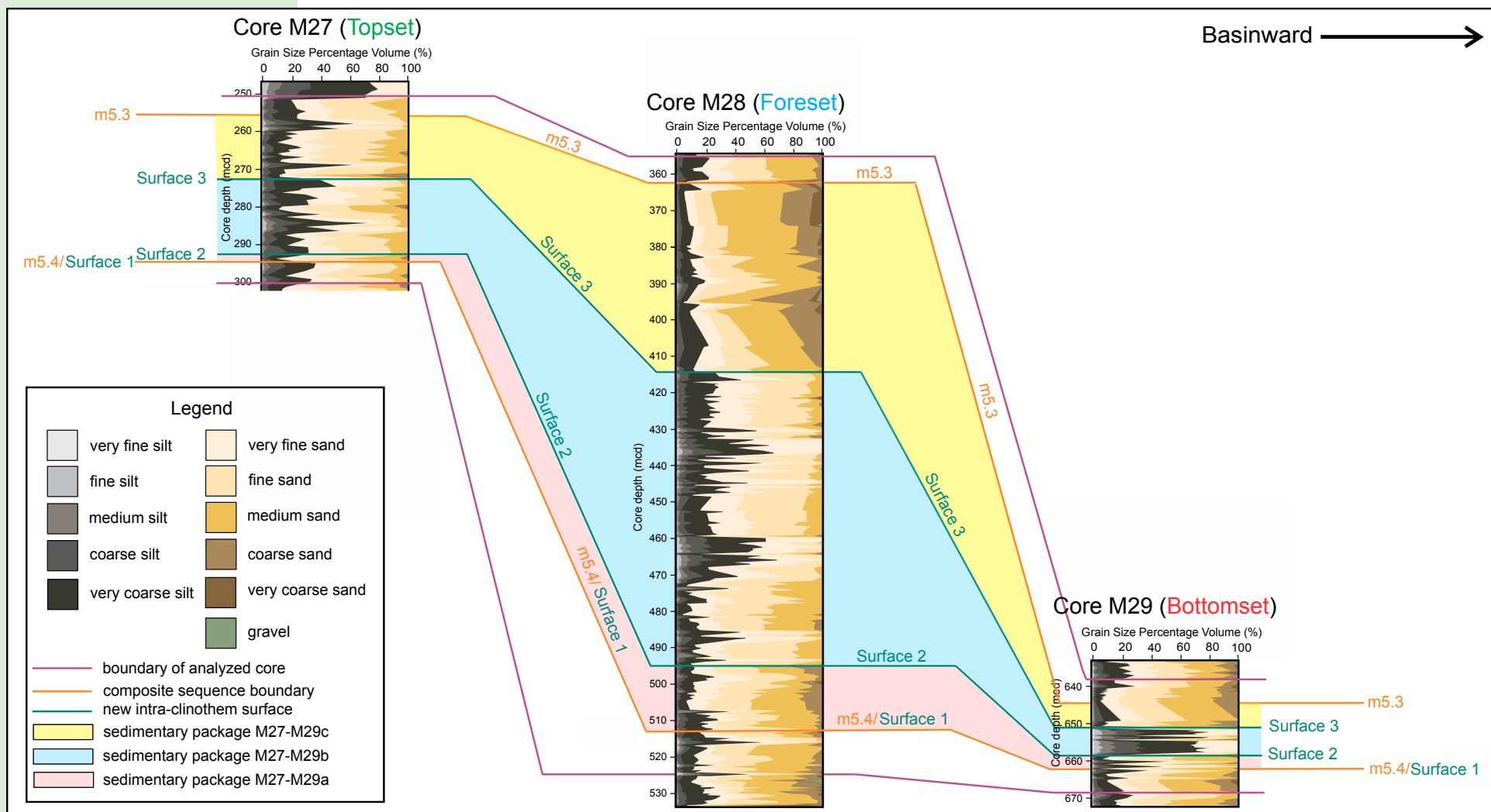


Figure 8. Correlation panel. The composite sequence boundaries (m5.4 and m5.3), as presented in Miller et al. (2013a), are shown in orange. Sedimentary package M27–M29a is highlighted in pink. Sedimentary package M27–M29b is highlighted in blue. Sedimentary package M27–M29c is highlighted in yellow. New interpreted intraclinothem surfaces (surface 1, surface 2, and surface 3) are shown in green. The interpreted surfaces are overlain onto new cumulative grain-size data presented in this investigation. The boundaries of the additional core described below and above the m5.4 and m5.3 sequence boundaries, respectively, are shown in purple. The core depth is also shown (mcd—meters composite depth).

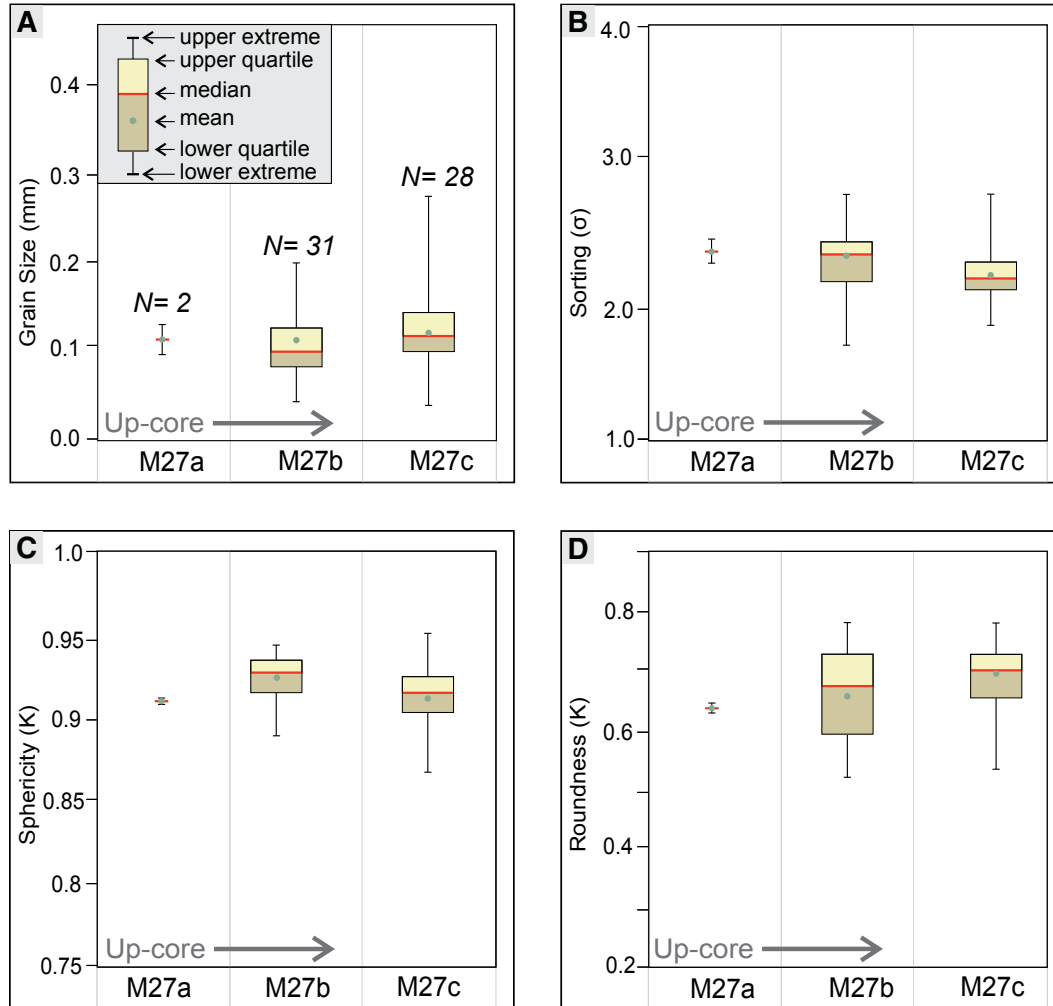


Figure 9. Box and whisker plots for sedimentary packages M27a, M27b, and M27c (topset deposits): (A) grain size; (B) sorting; (C) sphericity; and (D) roundness. Legend is shown in part A. Number of samples used to produce each box and whisker plot is shown in A by N = X. Due to the low sample number for M27a, only the mean, median, and standard deviation are shown.

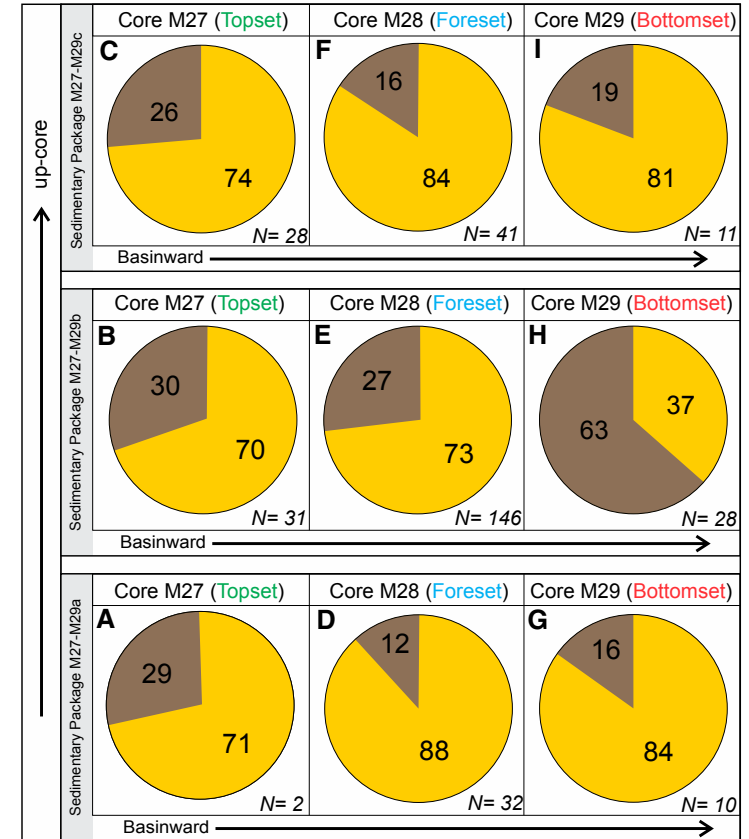


Figure 10. Pie charts showing average sand-to-mud composition by percentage volume: (A) sedimentary package M27a (topset); (B) sedimentary package M27b (topset); (C) sedimentary package M27c (topset); (D) sedimentary package M28a (foreset); (E) sedimentary package M28b (foreset); (F) sedimentary package M28c (foreset); (G) sedimentary package M29a (bottomset); (H) sedimentary package M29b (bottomset); (I) sedimentary package M29c (bottomset). Number of samples used to produce each pie-chart is shown by N = X.

TABLE 4. SUMMARY OF QUANTITATIVE GRAIN-CHARACTER DATA FOR SEDIMENTARY PACKAGES M27A–M27C

Core M27 (topset)					
Sedimentary package M27a		Sedimentary package M27b		Sedimentary package M27c	
Number of samples	2	Number of samples	31	Number of samples	28
Mean grain size (mm)	0.103	Mean grain size (mm)	0.106	Mean grain size (mm)	0.123
Median grain size (<i>n</i> 50) (mm)	0.103	Median grain size (<i>n</i> 50) (mm)	0.099	Median grain size (<i>n</i> 50) (mm)	0.119
Maximum grain size (mm)	0.118	Maximum grain size (mm)	0.198	Maximum grain size (mm)	0.271
Minimum grain size (mm)	0.087	Minimum grain size (mm)	0.044	Minimum grain size (mm)	0.042
Standard deviation (σ)	0.223	Standard deviation (σ)	0.040	Standard deviation (σ)	0.049
Mean sorting (σ)	2.345	Mean sorting (σ)	2.283	Mean sorting (σ)	2.204
Median sorting (<i>n</i> 50) (σ)	2.345	Median sorting (<i>n</i> 50) (σ)	2.326	Median sorting (<i>n</i> 50) (σ)	2.158
Maximum sorting (σ)	2.455	Maximum sorting (σ)	2.739	Maximum sorting (σ)	2.747
Minimum sorting (σ)	2.235	Minimum sorting (σ)	1.699	Minimum sorting (σ)	1.830
Standard deviation (σ)	0.156	Standard deviation (σ)	0.245	Standard deviation (σ)	0.196
Mean sphericity (K)	0.919	Mean sphericity (K)	0.922	Mean sphericity (K)	0.912
Median sphericity (<i>n</i> 50) (K)	0.919	Median sphericity (<i>n</i> 50) (K)	0.927	Median sphericity (<i>n</i> 50) (K)	0.916
Maximum sphericity (K)	0.921	Maximum sphericity (K)	0.943	Maximum sphericity (K)	0.949
Minimum sphericity (K)	0.917	Minimum sphericity (K)	0.888	Minimum sphericity (K)	0.867
Standard deviation (σ)	0.002	Standard deviation (σ)	0.016	Standard deviation (σ)	0.019
Mean roundness (K)	0.631	Mean roundness (K)	0.660	Mean roundness (K)	0.683
Median roundness (<i>n</i> 50) (K)	0.631	Median roundness (<i>n</i> 50) (K)	0.671	Median roundness (<i>n</i> 50) (K)	0.697
Maximum roundness (K)	0.654	Maximum roundness (K)	0.779	Maximum roundness (K)	0.776
Minimum roundness (K)	0.607	Minimum roundness (K)	0.519	Minimum roundness (K)	0.532
Standard deviation (σ)	0.033	Standard deviation (σ)	0.078	Standard deviation (σ)	0.059

TABLE 5. SUMMARY OF QUANTITATIVE GRAIN-CHARACTER DATA FOR SEDIMENTARY PACKAGES M28A–M28C

Core M28 (foreset)					
Sedimentary package M28a		Sedimentary package M28b		Sedimentary package M28c	
Number of samples	32	Number of samples	146	Number of samples	41
Mean grain size (mm)	0.174	Mean grain size (mm)	0.112	Mean grain size (mm)	0.238
Median grain size (<i>n</i> 50) (mm)	0.181	Median grain size (<i>n</i> 50) (mm)	0.111	Median grain size (<i>n</i> 50) (mm)	0.210
Maximum grain size (mm)	0.214	Maximum grain size (mm)	0.235	Maximum grain size (mm)	0.429
Minimum grain size (mm)	0.092	Minimum grain size (mm)	0.039	Minimum grain size (mm)	0.124
Standard deviation (σ)	0.040	Standard deviation (σ)	0.042	Standard deviation (σ)	0.068
Mean sorting (σ)	2.475	Mean sorting (σ)	2.148	Mean sorting (σ)	2.411
Median sorting (<i>n</i> 50) (σ)	2.445	Median sorting (<i>n</i> 50) (σ)	2.074	Median sorting (<i>n</i> 50) (σ)	2.436
Maximum sorting (σ)	3.837	Maximum sorting (σ)	3.667	Maximum sorting (σ)	2.807
Minimum sorting (σ)	2.132	Minimum sorting (σ)	1.633	Minimum sorting (σ)	1.953
Standard deviation (σ)	0.294	Standard deviation (σ)	0.258	Standard deviation (σ)	0.229
Mean sphericity (K)	0.887	Mean sphericity (K)	0.922	Mean sphericity (K)	0.915
Median sphericity (<i>n</i> 50) (K)	0.888	Median sphericity (<i>n</i> 50) (K)	0.924	Median sphericity (<i>n</i> 50) (K)	0.914
Maximum sphericity (K)	0.910	Maximum sphericity (K)	0.962	Maximum sphericity (K)	0.941
Minimum sphericity (K)	0.780	Minimum sphericity (K)	0.847	Minimum sphericity (K)	0.898
Standard deviation (σ)	0.023	Standard deviation (σ)	0.019	Standard deviation (σ)	0.008
Mean roundness (K)	0.522	Mean roundness (K)	0.651	Mean roundness (K)	0.581
Median roundness (<i>n</i> 50) (K)	0.532	Median roundness (<i>n</i> 50) (K)	0.645	Median roundness (<i>n</i> 50) (K)	0.568
Maximum roundness (K)	0.591	Maximum roundness (K)	0.800	Maximum roundness (K)	0.735
Minimum roundness (K)	0.326	Minimum roundness (K)	0.293	Minimum roundness (K)	0.491
Standard deviation (σ)	0.057	Standard deviation (σ)	0.070	Standard deviation (σ)	0.053

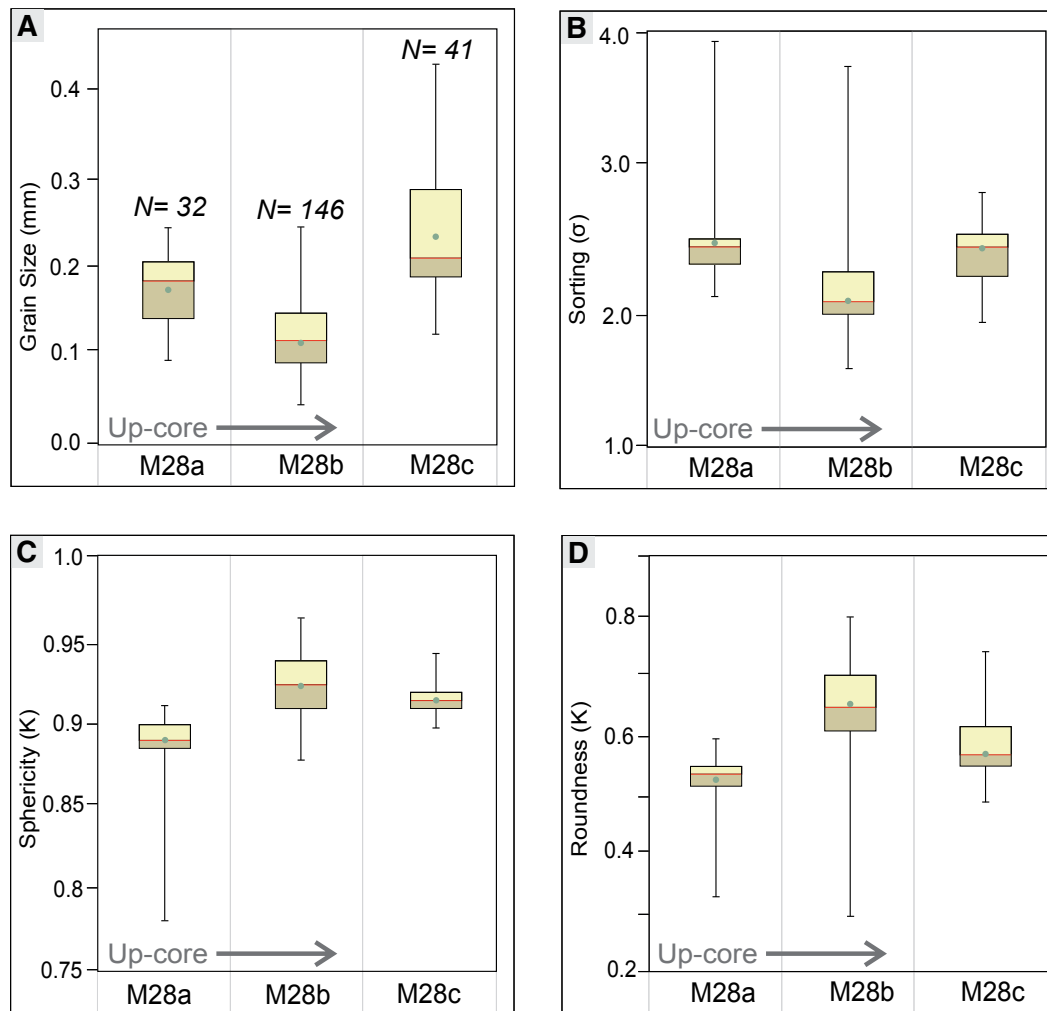


Figure 11. Box and whisker plots for sedimentary packages M28a, M28b, and M28c (foreset deposits): (A) grain size; (B) sorting; (C) sphericity; and (D) roundness. Legend is shown in Figure 9A. Number of samples used to produce each box and whisker plot is shown in part A by $N = X$.

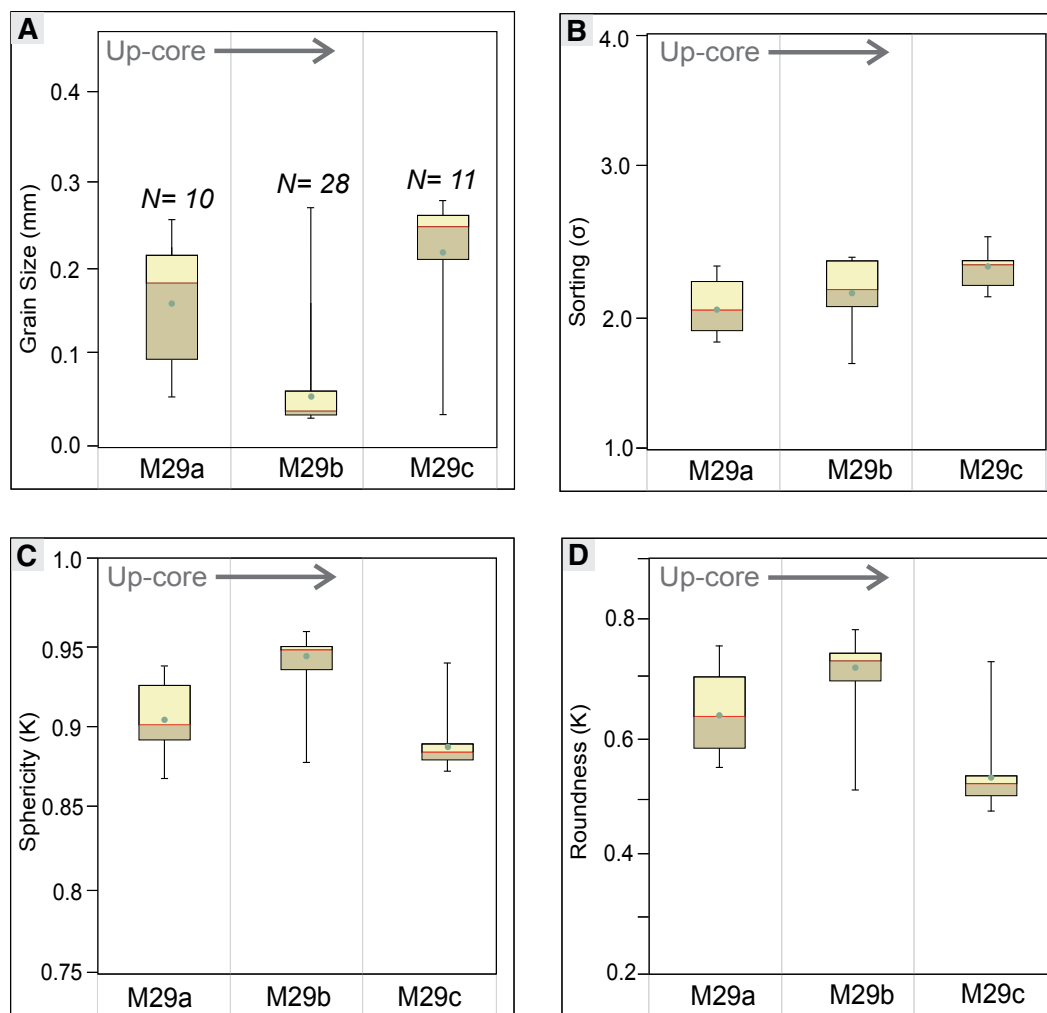


Figure 12. Box and whisker plots for sedimentary packages M29a, M29b, and M29c (bottomset deposits): (A) grain size; (B) sorting; (C) sphericity; and (D) roundness. Legend is shown in Figure 9A. Number of samples used to produce each box and whisker plot is shown in part A by $N = X$.

TABLE 6. SUMMARY OF QUANTITATIVE GRAIN-CHARACTER DATA FOR SEDIMENTARY PACKAGES M29A–M29C

Core M29 (bottomset)					
Sedimentary package M29a		Sedimentary package M29b		Sedimentary package M29c	
Number of samples	10	Number of samples	28	Number of samples	11
Mean grain size (mm)	0.156	Mean grain size (mm)	0.056	Mean grain size (mm)	0.212
Median grain size (<i>n</i> 50) (mm)	0.177	Median grain size (<i>n</i> 50) (mm)	0.037	Median grain size (<i>n</i> 50) (mm)	0.239
Maximum grain size (mm)	0.243	Maximum grain size (mm)	0.259	Maximum grain size (mm)	0.267
Minimum grain size (mm)	0.054	Minimum grain size (mm)	0.033	Minimum grain size (mm)	0.035
Standard deviation (σ)	0.073	Standard deviation (σ)	0.055	Standard deviation (σ)	0.068
Mean sorting (σ)	2.066	Mean sorting (σ)	2.158	Mean sorting (σ)	2.308
Median sorting (<i>n</i> 50) (σ)	2.040	Median sorting (<i>n</i> 50) (σ)	2.173	Median sorting (<i>n</i> 50) (σ)	2.347
Maximum sorting (σ)	2.341	Maximum sorting (σ)	2.388	Maximum sorting (σ)	2.533
Minimum sorting (σ)	1.834	Minimum sorting (σ)	1.687	Minimum sorting (σ)	2.130
Standard deviation (σ)	0.214	Standard deviation (σ)	0.151	Standard deviation (σ)	0.118
Mean sphericity (K)	0.907	Mean sphericity (K)	0.940	Mean sphericity (K)	0.890
Median sphericity (<i>n</i> 50) (K)	0.903	Median sphericity (<i>n</i> 50) (K)	0.947	Median sphericity (<i>n</i> 50) (K)	0.885
Maximum sphericity (K)	0.936	Maximum sphericity (K)	0.959	Maximum sphericity (K)	0.940
Minimum sphericity (K)	0.869	Minimum sphericity (K)	0.879	Minimum sphericity (K)	0.873
Standard deviation (σ)	0.024	Standard deviation (σ)	0.019	Standard deviation (σ)	0.018
Mean roundness (K)	0.644	Mean roundness (K)	0.713	Mean roundness (K)	0.540
Median roundness (<i>n</i> 50) (K)	0.637	Median roundness (<i>n</i> 50) (K)	0.732	Median roundness (<i>n</i> 50) (K)	0.519
Maximum roundness (K)	0.751	Maximum roundness (K)	0.782	Maximum roundness (K)	0.722
Minimum roundness (K)	0.549	Minimum roundness (K)	0.508	Minimum roundness (K)	0.475
Standard deviation (σ)	0.084	Standard deviation (σ)	0.058	Standard deviation (σ)	0.075

Sedimentary Package M27–M29a (River-Dominated Topset Deposits; Coarse-Grained Facies)

A downdip transect through sedimentary package M27–M29a, which is bounded by surface 1 (m5.4 sequence boundary of Miller et al., 2013a) and surface 2 (Fig. 8), reveals the following: (1) an increase in mean grain size from topset (0.14 mm) to foreset (0.16 mm) to bottomset (0.16 mm) deposits (Fig. 13A); (2) an increase in sorting from foreset (2.4σ) to bottomset (2.0σ) deposits (Fig. 13B); (3) the lowest sphericity and most angular grains retained in foreset deposits (Figs. 13C and 13D); (4) consistently bimodal grain-size distribution throughout the depositional profile that varies minimally downdip (Fig. 7J); and (5) an increasing sand-to-mud ratio from topset (71:29; Fig. 10A) through to foreset (88:12; Fig. 10D) and bottomset (84:16; Fig. 10G) deposits.

Sedimentary Package M27–M29b (Mixed Wave- and Storm-Dominated Topset Deposits; Fine-Grained Facies)

The downdip profile of sedimentary package M27–M29b, which is bounded by surfaces 2 and 3 (Fig. 8), reveals the following: (1) a decrease in mean grain size from topset (0.11 mm) and foreset (0.11 mm) to bottomset deposits (0.061 mm; Fig. 14A); (2) an increase in sorting from topset to foreset and bottomset deposits (Fig. 14B); (3) an increase in sphericity and roundness downdip (Figs. 14C and

14D); (4) a grain-size distribution that is consistently unimodal and narrows and fines downdip (Fig. 7K); and (5) a variable sand-to-mud ratio from topset (30:70; Fig. 10B) through foreset (27:73; Fig. 10E) to bottomset deposits (37:63; Fig. 10H).

Sedimentary Package M27–M29c (River-Dominated Topset Deposits; Coarse-Grained Facies)

The downdip profile of sedimentary package M27–M29c, which is bounded by surface 3 and the overlying m5.3 sequence boundary (Miller et al., 2013a; see also Fig. 8 herein), reveals the following: (1) The coarsest grain sizes (0.24 mm) are found within foreset deposits relative to topset (0.13 mm) and bottomset (0.21 mm) deposits (Fig. 15A); (2) the most poorly sorted deposits are retained in the foreset deposits (Fig. 15B); (3) the least spherical and most angular grains are found within bottomset deposits (Fig. 15C and 15D); (4) the average grain-size distribution is consistently bimodal and varies minimally downdip (Fig. 7L); and (5) the sand-to-mud ratio is lowest in topset deposits (26:74; Fig. 10C) and varies by <5% between foreset (84:16; Fig. 10F) and bottomset (81:19; Fig. 10I) deposits.

In summary, sedimentary package M27–M29b displays: (1) a finer mean grain size; (2) better sorting; and (3) higher mean values of sphericity and roundness, and it consistently displays a unimodal average grain-size distribution (Figs. 7 and 8) relative to sedimentary packages M27–M29a and M27–M29c. The foreset and bottomset deposits of sedimentary package M27–M29b are

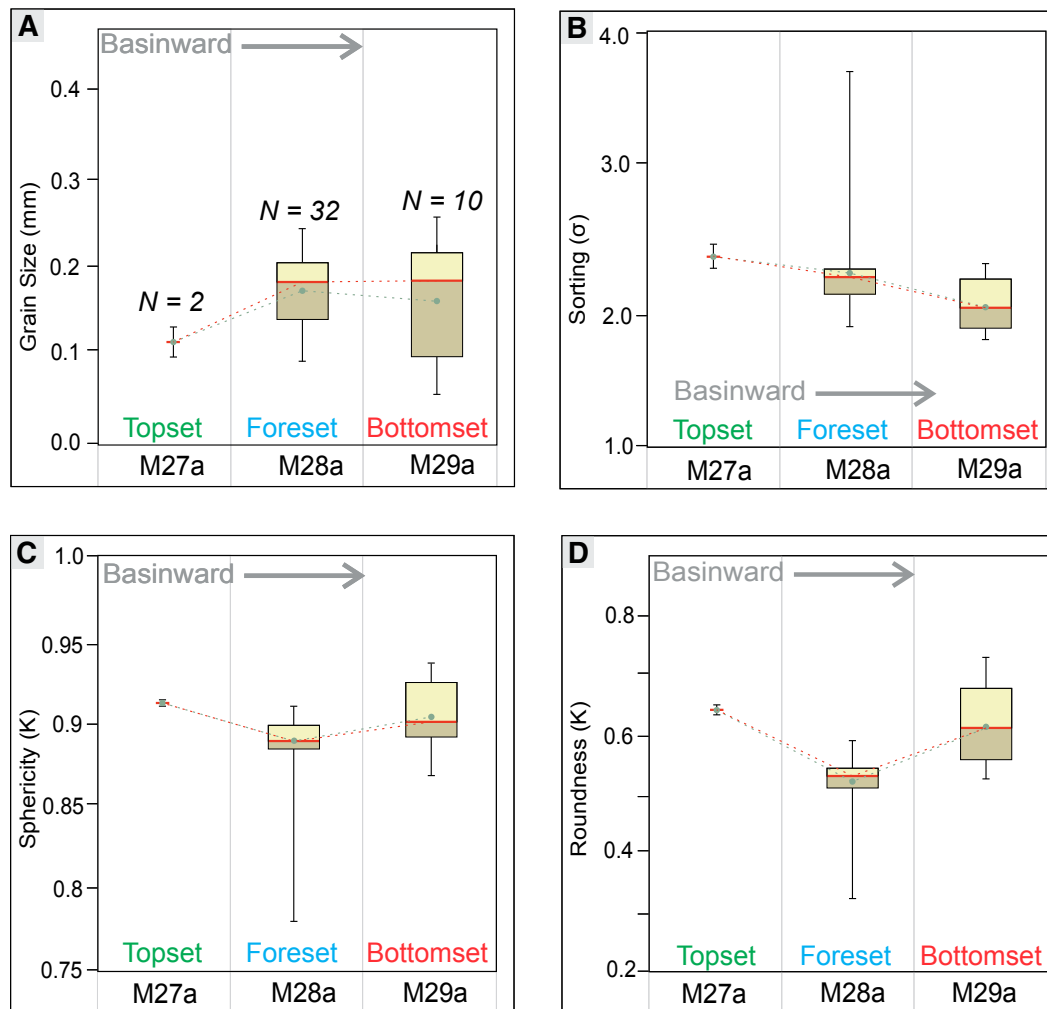


Figure 13. Box and whisker plots for sedimentary packages M27–M29a (topset–bottomset profile): (A) grain size; (B) sorting; (C) sphericity; and (D) roundness. Legend is shown in Figure 9A. Number of samples used to produce each box and whisker plot is shown in part A by $N = X$. Due to the low sample number for M27a, only the mean, median, and standard deviation are shown.

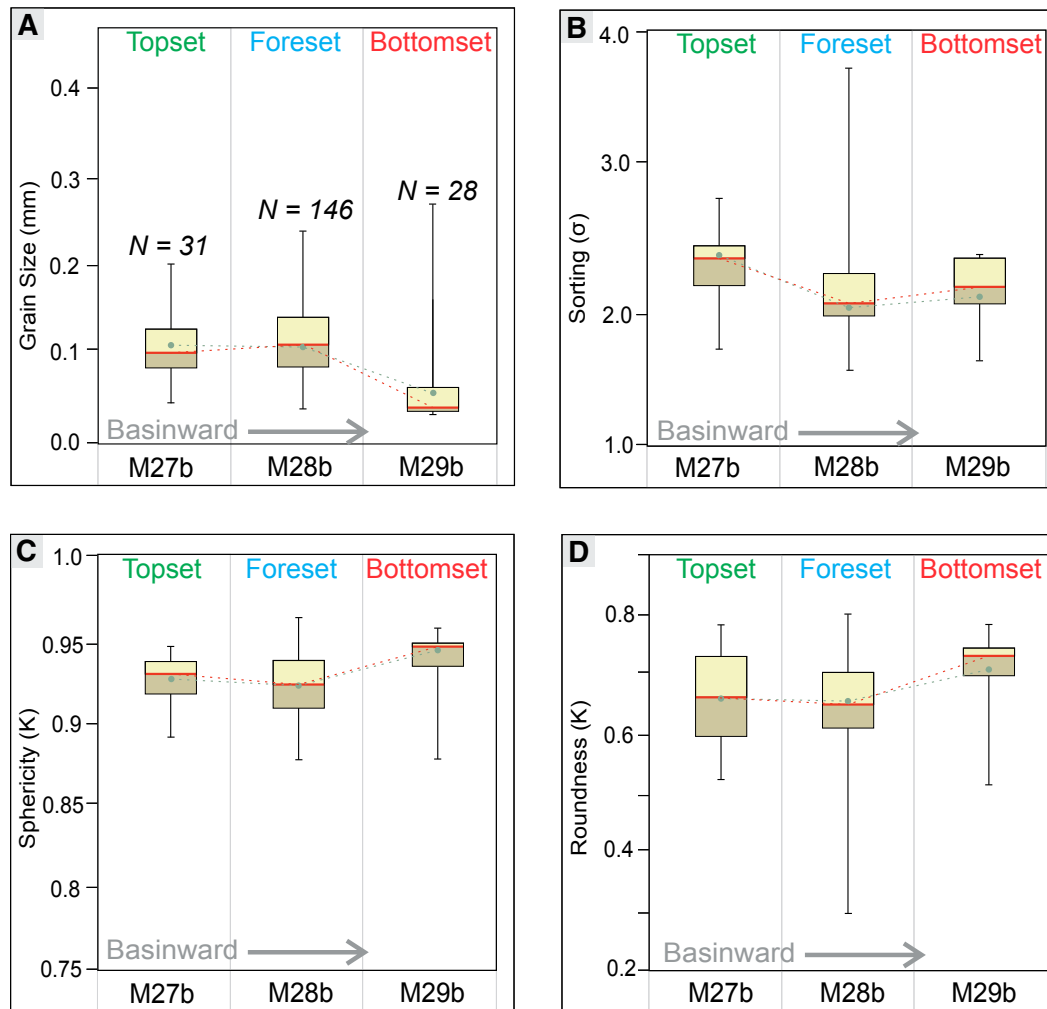


Figure 14. Box and whisker plots for sedimentary packages M27–M29b (topset-bottomset profile): (A) grain size; (B) sorting; (C) sphericity; and (D) roundness. Legend is shown in Figure 9A. Number of samples used to produce each box and whisker plot is shown in part A by $N = X$.

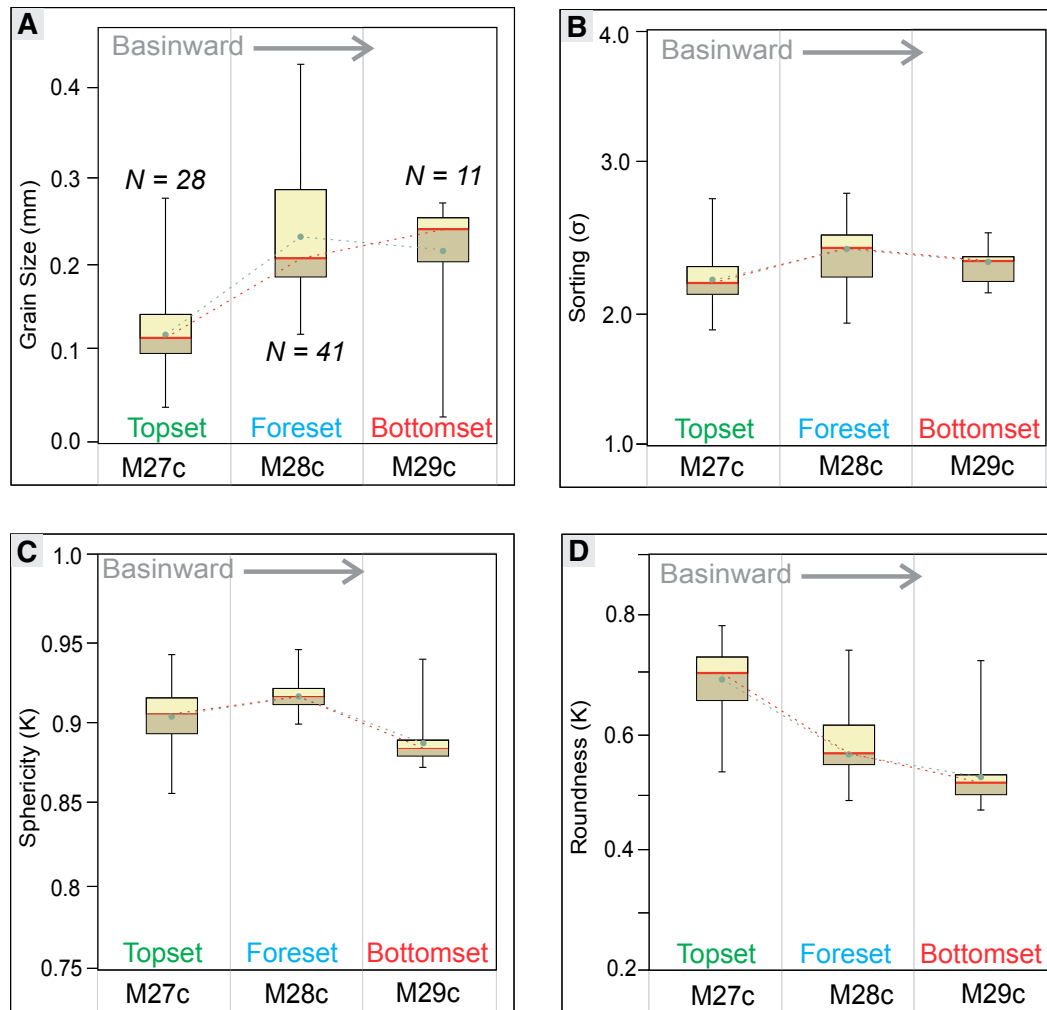


Figure 15. Box and whisker plots for sedimentary packages M27–M29c (topset-bottomset profile): (A) grain size; (B) sorting; (C) sphericity; and (D) roundness. Legend is shown in Figure 9A. Number of samples used to produce each box and whisker plot is shown in part A by $N = X$.

significantly more mud-prone relative to sedimentary packages M27–M29a and M27–M29c, which contain >80% sand (Fig. 10).

Up-Core Grain-Size Patterns

The new high-resolution, quantitative grain-size data presented in this investigation are shown in Figure 8.

Site M27

From 300.00 mcd to 295.00 mcd, the dominant grain size is fine-grained sand, which typically makes up ~60% of the total grain-size composition. At 298.19 mcd, the grain size coarsens abruptly, associated with an increase in the medium sand content from ~10% to ~30%, and the introduction of coarse sand, which forms ~7% of the overall grain-size composition. At 295.00 mcd, there is the surface 1 to m5.4 sequence boundary (Miller et al., 2013a), which is overlain by a sand-rich package, and an abrupt increase in the medium sand content (Fig. 8). The coarse-grained sandy package (composed of ~45% and ~10% medium- and coarse-grained sand, respectively) terminates at 294.26 mcd (surface 2). Directly overlying surface 2, there is an increase in the overall silt content (from ~15% to ~30%) and a decrease in the medium sand content (from ~45% to ~10%) within a fining-upward trend (294.26–285.06 mcd); this is overlain by a coarsening-upward package (285.05–279.78 mcd). A final fining-upward package (279.78–272.99 mcd) terminates at surface 3 (272.99 mcd; this study). Surface 3 is marked by a decrease in silt content (~55% to ~18%) and increase in coarse and very coarse sand, which form ~30% of the total sediment composition. Grain-size trends overlying surface 3 show a general fining-upward motif (272.98–256.19 mcd), which terminates at the overlying sequence boundary m5.3 (256.19 mcd). Overlying the Miller et al. (2013b) m5.3 sequence boundary, there is general coarsening-upward trend to 251 mcd, and there is an increase in the medium sand content from ~5% below the m5.3 sequence boundary to a maximum of ~25% at 251.52 mcd (Fig. 8).

Site M28

From 525.00 to 519.70 mcd, there is a fining-upward sandy package, which typically consists of ~35% medium sand. At 519.70 mcd (alternative m5.4 sequence boundary as proposed by Hodgson et al., 2018), there is a marked increase in medium sand content (~55%). From 519.70 to 515.89 mcd, there is a fining-upward trend that results in an increase in the overall silt content from ~12% at 516.80 mcd to ~52% at 514.74 mcd (Fig. 8). From 514.71 to 512.33, there is a general coarsening-upward trend. The 512.33 mcd sequence boundary (Miller et al., 2013a) is shared by surface 1 (this study) and directly overlies a very coarse sand at 512.97 mcd. Grain-size trends overlying surface 1 show a general coarsening-upward trend to 495.00 mcd (surface M28b; this study). Surface 2 is

associated with an overlying fining in mean grain size and the disappearance of the coarse sand fractions. Surface 1 corresponds with the placement of the original m5.4 surface identified in Mountain et al. (2010) at 495.20 mcd, where a thin sand bed overlies a clayey silt. Grain-size trends overlying surface 2 show two fining-upward packages (495.00–459.95 and 459.94–432.00 mcd), which are overlain by a package of fine sand (432.00–415.00 mcd) that terminates at surface 3 (415.00 mcd; this study). Surface 3 is associated with a marked increase in medium sand content from ~7% to ~45% of the total sediment composition. Overlying surface 3, there are two coarsening-upward packages (415.00–392.00 and 392.00–363.00 mcd), which terminate at sequence boundary m5.3 (363.00 mcd; Miller et al., 2013a). Directly overlying the m5.3 sequence boundary, the gravel and very coarse sand are no longer present. From 363.00 to 358.00 mcd, the grain-size composition is dominated by fine and medium sand (Fig. 8).

Site M29

From 667.00 to 662.37 mcd, there is a general fining-upward trend; at this stratigraphic interval, the grain-size composition is dominated by fine and medium sand. At 662.37 mcd, there is the m5.4 sequence boundary (Miller et al., 2013a), shared by surface 1 (this study). Directly overlying surface 1, there is a decrease in silt content from ~50% to ~12% and an increase in the medium sand content from ~10% to ~60%. From 662.37 to 658.50 mcd, there is a sedimentary package dominated by medium sand, which forms ~50% of the total sediment composition (Fig. 8). The sand-rich package terminates at surface 2 (658.50 mcd; this study). Directly overlying surface 2, there is a marked increase in the silt content (from ~5% to ~75%). Overlying surface 2, the grain size is dominated by silts (658.50–651.64 mcd), which form ~60% to ~80% of the total sediment composition; the silts are occasionally punctuated by thin lenses of medium and coarse sand (Fig. 8). The silt-rich package terminates at surface 3 (651.64 mcd). Directly overlying surface 3, the silt content drops from ~75% to ~5%, and coarse sand is present, forming ~25% of the total sediment composition. Overlying surface 3, there is a fining-upward trend (651.64–649.51 mcd), followed by a coarsening-upward package (649.50–643.19 mcd), which terminates at the overlying sequence boundary m5.3 (643.19 mcd). From 643.19 to 638.00 mcd, there is an overall fining-upward trend (Fig. 8).

DISCUSSION

How Does Intraclinothem Topset Process Regime Influence Downdip Grain Character?

Vertical Process Variability and Grain Character

The core expression of sequence m5.4 topset deposits indicates that either fluvial-dominated (M27a and M27c) or wave- and storm-dominated (M27b)

processes were active within the same seismic sequence. The presence of both fluvial and wave-and-storm process regimes within one seismic sequence indicates that sequence m5.4 is an example of a mixed-energy system (e.g., Ainsworth et al., 2008, 2011; Olariu, 2014; Gomis-Cartesio et al., 2017), rather than a clinothem described by a single process regime (see examples cited in Dixon et al., 2012a). Concomitant changes in quantitative grain character occur in association with changes in the dominant process regime.

River-Dominated Sedimentary Packages

The sand-to-mud ratios show river-dominated sedimentary packages are dominated by bypass of sand-grade sediment across topsets and preferential deposition within foreset and bottomset deposits (Fig. 10). The shapes of the grain-size distribution profiles vary minimally between foreset and bottomset deposits (Figs. 7J and 7L); this suggests the bulk transfer of sand fractions across topsets. However, the foreset deposits are relatively coarser, indicating preferential deposition of the coarser grain-size fractions (0.25–0.75 mm; medium- and coarse-grained sand) in the slope setting. This may reflect the rapid dissipation of gravity-flow energy, resulting in slope deposition of the coarsest grain-size classes.

The high sand-to-mud ratios are associated with debritic and turbiditic foreset and bottomset deposits, which are typically glauconite-bearing sands. The association between reworked glauconite and river-dominated topsets was documented by Mountain et al. (2010), who interpreted clinof orm sequences that had poorly sorted glauconitic sand in the clinof orm rollover position as river-dominated features. The presence of recycled glauconite within foreset and bottomset deposits supports topset glauconitic sands as a sediment source for downdip deposits (Hodgson et al., 2018; Proust et al., 2018).

Although the sand content is relatively high within the river-dominated sedimentary packages, river-dominated deposits are less well sorted, and grain shapes tend to be less spherical and more angular than that of the wave- and storm-dominated sedimentary package (Figs. 13, 14, and 15). The lower textural maturity of the river-dominated deposits reflects a shorter transport time from hinterland erosion to deposition within foreset and bottomset deposits (Hodgson et al., 2018).

The river-dominated deposits exhibit a consistent bimodality in average grain-size distribution (Figs. 7J and 7L), which suggests a dual sediment source. This is interpreted to reflect a fine sand component associated with hinterland erosion and a coarser glauconite sand component associated with reworking from topset and clinof orm rollover deposits. The bimodality in average grain-size distribution is present throughout the topset to bottomset profile in both river-dominated packages (Figs. 7J and 7L). In both cases, there is a slight coarsening from topset to foreset deposits, and then the average grain-size distribution remains constant between foreset and bottomset deposits (Figs. 7J and 7L). The coarsest grains are not sequestered in topset deposits, suggesting bypass of the coarsest-grained sediment fractions, possibly through

channels. The average grain-size distribution profile of the river-dominated deposits reflects sourcing of the coarsest grain-size fractions (typically reworked glauconite and quartz) from the clinof orm rollover seaward of the core M27 intersection. Additionally, the average grain-size distribution profiles also indicate relatively efficient sediment transport beyond the shelf break, associated with sediment bypass (cf. Stevenson et al., 2015).

Wave- and Storm-Dominated Sedimentary Packages

The sand-to-mud ratios of the wave- and storm-dominated sedimentary package (M27–M29b) are consistently lower than those of the river-dominated packages; the difference in sand content becomes greater downdip, where the bottomsets of the river-dominated packages contain up to 47% more sand than the wave- and storm-dominated sedimentary package (Fig. 10). The sand-to-mud ratios of the wave- and storm-dominated sedimentary package show the retention of sand-grade sediment within topset and foreset deposits, with limited basinward sand bypass (Fig. 10). The bottomset deposits are associated with mud-grade sediment, attributed to deposition from suspension fallout. Compared to the river-dominated deposits, the foreset and bottomset deposits of the wave- and storm-dominated sedimentary package are less sand-rich (foreset and bottomset deposits contain an average of 13% and 45.5% less sand, respectively; Fig. 10), but the textural maturity is higher (Figs. 13, 14, and 15). The relatively higher textural maturity displayed by the wave- and storm-dominated deposits reflects reworking processes landward of the shelf edge, associated with the redistribution of sediment and a longer residence time within the sediment transport system (Bhattacharya and Walker, 1992; Diebert et al., 2003; Li et al., 2011). The downdip average grain-size distribution profiles of wave and storm deposits display prominent fining from topset to bottomset (Fig. 7K). This reflects the inefficiency of wave- and storm-dominated systems at transferring sand beyond the shelf edge, and the dominance of shore-parallel sediment redistribution (Coleman and Wright, 1975; Bhattacharya and Giosan, 2003), resulting in relatively thick, sand-prone topset deposits. The documentation of significant variability in sediment composition and texture within the bottomset deposits of a single clinothem sequence suggests that nuanced changes in topset process regime may represent a hitherto overlooked contributing factor in the depositional evolution of clinothem sequences.

Lateral Variability in Process Regime

The core data set presented here is from a single 2-D dip-parallel transect and captures only one portion of the along-strike variability; however, a network of 2-D seismic reflection lines permits the three-dimensional (3-D) architecture of sequence m5.4 to be constrained (Monteverde et al., 2008). Recent studies have highlighted that shallow-marine systems, both modern

and ancient, can display prominent lateral variability associated with changes in the interactions among fluvial, wave, and tidal processes (Ta et al., 2002; Ainsworth et al., 2008, 2011; Olariu, 2014; Jones et al., 2015).

The propensity for systems to exhibit lateral variability, associated with changes in the dominant process regime, has the potential to increase grain-character heterogeneity both along strike and downdip. In the context of improved prediction of downdip facies from updip sedimentary facies, the interactions of temporal and lateral process-regime change could introduce significant variability not only in sand content, but also in grain character. For example, the influence of shore-parallel variability may be expressed as a lateral transition from a river-dominated topset system to a wave-dominated system further along strike; however, downdip of the wave-dominated system, a fan fed by the river-dominated system could be intersected.

Despite this, sequence m5.4 is a rare example of a chronostratigraphically constrained clinothem, in which the sedimentological and stratigraphic characteristics of coeval topset, foreset, and bottomset deposits have been documented. Future studies of the relationship between along-strike variability in process regime and grain-character variability will require exceptional outcrop control, or integrated 3-D seismic reflection data sets and core-hole data with strike and dip control.

Classification of Mixed Process-Regime Clinothems

Cosgrove et al. (2018) determined that sequence m5.4 formed a rising clinoform trajectory and was a wave-dominated feature. Across seismic sequence m5.4, the majority of the cored topset, foreset, and bottomset deposits preserve indicators consistent with wave-dominated topset deposits, including minimal transport of coarse-grained sediment into deep-water settings (e.g., Helland-Hansen and Hampson, 2009). However, designating the entire sequence as belonging to this end-member category fails to accurately describe the stratigraphic or geographic variability. The stratigraphic intervals in sequence m5.4 that have a river-dominated topset process regime (sedimentary correlations M27–M29a and M27–M29c) are associated with the effective transport of coarse sand into the deep-water setting. Therefore, characterizing a clinothem by a single process or a clinoform trajectory fails to account for the inherent stratigraphic and lateral variability in mixed process-regime systems.

Autogenic and Allogenic Topset Process-Regime Change

The cause of changes in topset process regime may be controlled by allogenic or autogenic forcing mechanisms. Allogenic controls, i.e., those which are external to the sedimentary unit, primarily document the effects of eustatic variability and changes in hinterland climatic and tectonic regime, which modulate the production and discharge of sediment from source regions (e.g., Castelltort and Van Den Driessche, 2003; Armitage et al., 2011). The effects of

allogenic forcing mechanisms could feasibly result in changes in the topset process regime and consequently account for the stratigraphic expression of the surfaces and sedimentary packages displayed in sequence m5.4. The scenario in which allogenic processes result in the observed intraclinotem surfaces, in addition to their regional basinward extent, would support their interpretation as sequence boundaries within a m5.4 composite sequence (Miller et al., 2013a, 2013b; Miller et al., 2018).

The intraclinotem surfaces could also be the result of autogenic controls, such as river avulsion and/or switching of wave-dominated delta lobes (e.g., Olariu, 2014; Hampson, 2016); this would mean that the intraclinotem surfaces are not sequence boundaries. Autogenic mechanisms have been shown to generate surfaces and stratigraphic architectures that are challenging to distinguish from those generated through allogenic processes (e.g., Muto and Steel, 2002). The identification of autogenic and/or allogenic generation of the intraclinotem surfaces, in this instance, remains tentative given the lack of strike control to test the regional extent of the surfaces and resolution of the chronostratigraphic data.

How Can High-Resolution Grain Character Data Be Used as an Additional Correlation Tool?

Miller et al. (2013a) determined sequence m5.4 to be a composite sequence, composed of three higher-order sequences (m5.4-1, m5.34, m5.33) of ~100 k.y. duration. However, the placement of the intraclinotem stratigraphic surfaces was associated with varying degrees of uncertainty (Fig. 4). The placement of the intraclinotem sequence boundaries at Site M27 is primarily based on stacking pattern analysis. However, trends above the m5.33 sequence boundary are acknowledged to be unclear (Miller et al., 2013b). Furthermore, the Sr-isotope error margins and the single sample used to date sequence m5.33 (Browning et al., 2013) render the chronostratigraphic data weak.

At Site M28, sequence boundary m5.4-1 (17.7–17.6 Ma; Browning et al., 2013) is suggested to share its basal reflector with sequence boundary m5.4 (Miller et al., 2013a). Sequence boundary m5.34 (479.00 mcd; Miller et al., 2013a) is interpreted from seismic reflector terminations; however, only a minor impedance contrast, a weak core expression (Miller et al., 2013b), and no significant chronostratigraphic hiatus (Browning et al., 2013) are present. The placement of the m5.33 sequence boundary is based on the criteria of onlap and downlap (Miller et al., 2013a), which coincides with a coring gap (~405 mcd; Miller et al., 2013a). In light of the coring gap and the error associated with Sr-isotope data (± 0.61 – 0.4 m.y.; see Browning et al., 2013), the placement is ambiguous.

At Site M29, the correlation of sequence boundaries m5.4-1, m5.34, and m5.33 is more tentative. Sr-isotope data permit correlation with both the m5.4-1 and m5.34 sequence boundaries (17.7–17.6 Ma; Browning et al., 2013; Miller et al., 2013a). Additionally, there are weak/no core sequence boundaries proposed for m5.34 and m5.33, respectively, which, combined with chronostratigraphic data, provides unconvincing evidence for a composite sequence at M29.

Grain-character data provide an alternative approach to the subdivision of clinothems (Fig. 10). The alternative intraclinothem surfaces presented here were correlated across the complete depositional profile and correspond to changes in facies, grain size (Figs. 13–15), grain shape (Figs. 13–15), grain-size distribution (Fig. 7), sand-to-mud ratios (Fig. 10), and stratigraphic stacking pattern (Fig. 8). The placement of the intraclinothem surfaces in this investigation differs from those proposed previously (m5.4-1, m5.34, and m5.33; Miller et al., 2013a). The differences in the stratigraphic placement of the intraclinothem surfaces between previous investigations and this study are attributed to (1) the different methodologies used to identify the intraclinothem surfaces and (2) the stratigraphic resolution available to each investigation. The intraclinothem surfaces that separate the sedimentary packages presented in this investigation are attributed to changes in the dominant topset process regime. The results presented here highlight the potential application of quantitative grain-character data sets as supplementary correlation tools. Abrupt changes in grain size (many qualitatively observed) are widely used as a means of subdividing the stratigraphic record; however, additional grain-character attributes (including sorting, sphericity, and roundness) are overlooked. The lack of data sets that utilize sorting, sphericity, and roundness as additional correlation tools reflects the general lack of quantitative data sets in the wider literature.

How Can High-Resolution Grain Character Data Be Used as an Additional Tool to Refine Sequence Boundaries?

Different approaches exist for the placement of sequence boundaries across depositional profiles (e.g., Catuneanu et al., 2009; Hodgson et al., 2016; Barrett et al., 2018). However, in this instance, previous authors have followed a similar approach (Monteverde et al., 2008; Mountain et al., 2010; Miller et al., 2013a, 2013b; Hodgson et al., 2018; Miller et al., 2018) to place sequence boundaries within the Expedition 313 data set. Despite the integrated data set, which has identified sequence boundaries in multichannel seismic profiles and in core and sedimentary logs, uncertainty remains regarding the placement of the m5.4 sequence boundary (Fig. 4). At Site M28, sequence boundary m5.4 has been placed at 495.20 mcd by Mountain et al. (2010), at 512.33 mcd by Miller et al. (2013a), and an alternative at 519.70 mcd by Hodgson et al. (2018). The ambiguity surrounding the exact placement of the sequence boundary m5.4 is exacerbated by the absence of strong supporting seismic impedance contrast and chronostratigraphic data, and the nonuniqueness of core-based approaches to identify sequence boundaries (e.g., Browning et al., 2006). The surface of Mountain et al. (2010) corresponds to a thin sand bed overlying a clayey silt. The surface of Miller et al. (2013a) corresponds to a contact of fine sand overlying clayey silt; this is associated with a minor impedance contrast and a minimal chronostratigraphic time gap (ca. 17.9 Ma below and 17.7 Ma above). The alternative surface of Hodgson et al. (2018) corresponds to a bioturbated contact, where an upward-fining, sharp-based sand is overlain by silt.

Grain-Size Trends

Mountain et al. (2010), Miller et al. (2013a), and Hodgson et al. (2018) used abrupt changes in stacking patterns and grain size to aid placement of the m5.4 sequence boundary. The higher-resolution, fully quantitative grain-size data presented in this investigation reveal more detailed up-core grain-size trends and stacking patterns (Fig. 16). In the original semiquantitative cumulative lithology, the Hodgson et al. (2018) alternative sequence boundary (519.70 mcd) appears to immediately overlie a clay- and silt-rich horizon, which forms part of a fining-upward package. However, the candidate sequence boundary does not directly correspond with a prominent change in stacking pattern when the detailed cumulative grain-size data presented in this investigation are considered (Fig. 16). The new cumulative grain-size data do not indicate the presence of a large clay/silt peak directly underlying the proposed sequence boundary (Fig. 16). Instead, the total silt content remains relatively low (12%), and a more subtle increase in the very fine and fine sand content is observed. This subtle but significant difference in grain size is likely a product of the different (quantitative and semiquantitative) methodologies used in this investigation versus those presented in Miller et al. (2013b). The candidate sequence boundary proposed by Hodgson et al. (2018) does correspond with an increase in the medium sand content (30% and 47% directly below and above the proposed surface, respectively; Fig. 16). However, this does not correspond with an overall change in stacking pattern, as is suggested by the original semiquantitative cumulative lithology. The new data presented here place the candidate sequence boundary proposed by Hodgson et al. (2018) within a fining-upward package, which peaks at 515.89 mcd and corresponds with a large peak in the silt content. The ~1.5 m sampling interval used to produce the original semiquantitative cumulative lithology was not of sufficient resolution to capture this.

The candidate sequence boundary proposed by Mountain et al. (2010; 495.00 mcd) was placed using general lithology alone, and it was placed within a very fine to fine sand package. The new cumulative grain-size data presented here indicate that the candidate sequence boundary of Mountain et al. (2010) corresponds to a broad change in stacking pattern and falls where a coarsening-upward package (containing coarse and very coarse sand) abruptly transitions into a relatively finer-grained package (Fig. 16). The abrupt change in grain size at 495.00 mcd is interpreted to represent intraclinothem surface 2, associated with a change in the topset process regime and the depositional style associated with this change.

In the original semiquantitative cumulative lithology, the candidate sequence boundary proposed by Miller et al. (2013a; 512.33 mcd) appears to overlie a coarsening-upward package and was placed at the junction between a clay/silt peak and very fine/fine sand package (Fig. 16). The new cumulative grain-size data presented here show the same overall stacking pattern: a coarsening-upward package that terminates at the 512.33 mcd and is overlain by a blocky, sand-rich package. There is also a peak in the fine sand content (40% of the total sediment composition) directly overlying the candidate sequence

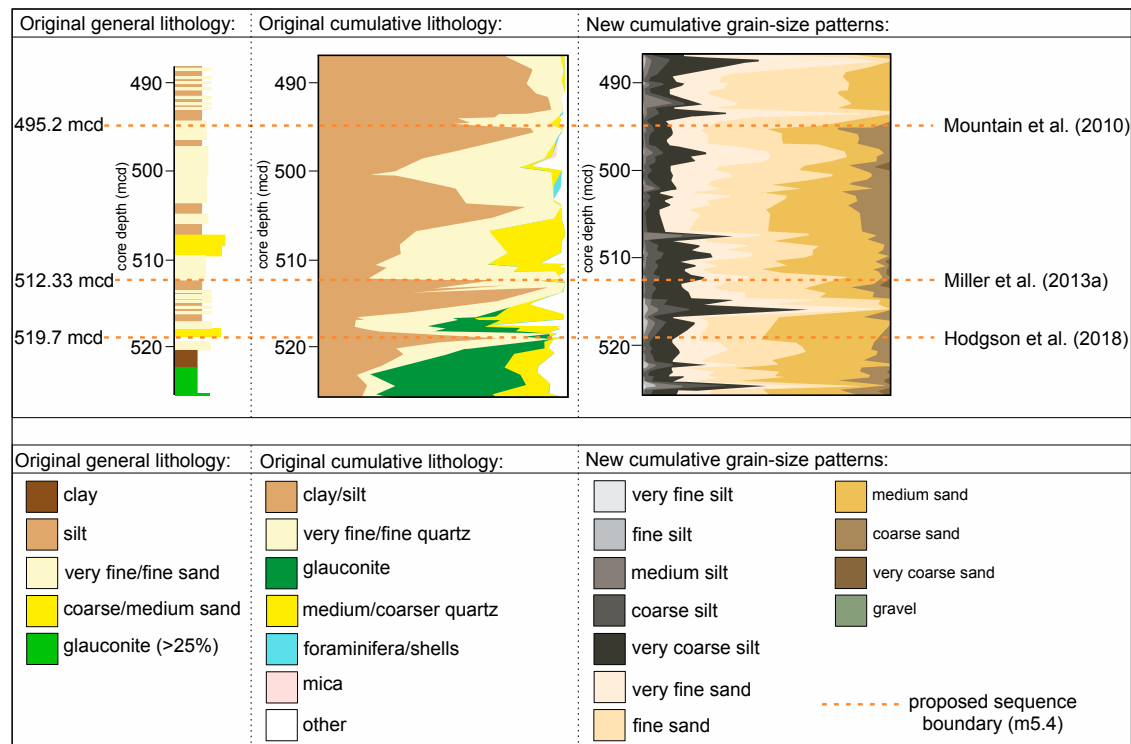


Figure 16. Comparison of the “original general lithology” (Mountain et al., 2010), “original cumulative lithology” (Miller et al., 2013b), and new cumulative grain-size patterns (this study). The candidate m5.4 sequence boundaries (from Mountain et al., 2010; Miller et al., 2013a; Hodgson et al., 2018) are overlain in dashed orange lines. The core depth is also shown (mcd—meters composite depth).

boundary of Miller et al. (2013a). The clay/silt content presented in the original semiquantitative cumulative lithology is significantly higher than that of the new high-resolution grain-size data; this is attributed to differences in technique used for data acquisition. The candidate sequence boundary at 512.33 mcd broadly corresponds with a change in stacking pattern across the original qualitative general lithology, the original semiquantitative cumulative lithology, and the new high-resolution grain-size data presented here, which supports this position as the m5.4 sequence boundary.

From the lower-resolution, semiquantitative cumulative lithology, it is clear that previous authors have identified potential sequence boundaries based upon perceived abrupt changes in grain size and lithology, alongside core-based criteria (Fig. 16). The higher-resolution quantitative data set presented here displays the same broad-scale (approximately tens of meters) trends in stacking as those presented by Mountain et al. (2010) and Miller et al. (2013b), but it refines and improves: (1) the accuracy of the grain-size composition and (2) the stratigraphic locations of changes in stacking pattern.

Grain Character

The fully quantitative nature of this data set enables changes grain size (including sand-to-mud content and mean grain size) to be calculated across the three candidate sequence boundaries. Of the three proposed sequence boundaries, the greatest change in sand-to-mud content occurs at the Miller et al. (2013a) boundary at 512.33 mcd, where a net change of 10% in sand-to-mud content is recorded, compared to 6.8% and 0.8% change at the boundaries of Mountain et al. (2010) and Hodgson et al. (2018), respectively (Fig. 17). In addition to the changes in sand-to-mud ratios, changes in mean grain size across the proposed sequence boundaries have been calculated (Fig. 18). The largest change in mean grain size across the three candidate sequence boundaries again occurs across the 512.33 mcd sequence boundary (Miller et al., 2013a), where a 29% change in mean grain size is observed, compared to a 20% and 18% change at the 495.20 mcd (Mountain et al., 2010) and 519.70 mcd (Hodgson et al., 2018) boundaries, respectively (Fig. 18A). One of the fundamental

tenets for determining sequence boundaries is based upon the identification of abrupt stratigraphic changes in grain size; hitherto, a quantitative assessment of these parameters has been unavailable due to the relatively low sampling densities and qualitative/semiquantitative methodologies employed by previous authors. Quantitative analysis of sand-to-mud ratios and mean grain-size changes across the three proposed sequence boundaries supports a preferred sequence boundary at 512.33 mcd (Miller et al., 2013b), which displays the greatest overall change in grain size (Figs. 17 and 18A).

Up-core grain-shape characteristics (sphericity and roundness; Figs. 18B and 18C) are also shown alongside the potential sequence boundaries proposed by Mountain et al. (2010), Miller et al. (2013a), and Hodgson et al. (2018). Similarly, the grain-shape data support placement of the Miller et al. (2013a) sequence boundary at 512.33 mcd. The grain shapes become increasingly angular and less spherical up core to the 512.33 mcd sequence boundary; at the 512.33 mcd sequence boundary, there is a significant drop in both grain sphericity (from 0.91 to 0.78; 15.5%) and grain roundness (from 0.61 to 0.33; 59.6%) to their lowest levels within the stratigraphic section (Fig. 18). The dramatic difference in grain shape across this stratigraphic horizon supports a fundamental change in sediment source and/or transport regime, consistent with a depositional hiatus and sequence boundary; this is supported by the core expression of the 512.33 mcd sequence boundary (see Miller et al., 2013a). The other candidate sequence boundaries exhibit significantly less change in grain shape across the proposed sequence boundaries: 1.8% and 5.5% change in roundness and 1.1% and 0.1% change in sphericity for the Mountain et al. (2010) and Hodgson et al. (2018) candidate sequence boundaries, respectively (Fig. 18).

The high-resolution grain-character data presented here may provide an additional, complementary approach, to be used in conjunction with core criteria, to refine the placement of sequence boundaries, and/or to determine the most statistically likely sequence boundary from a number of candidate sequence boundaries. Additionally, the higher-resolution up-core grain-size data presented here highlight the fact that lower-resolution, semiquantitative lithological data may dramatically oversimplify grain-size trends and promote the somewhat arbitrary placement of sequence boundaries in core sections.

CONCLUSIONS

Integrated grain-character data and core facies have been used to describe a mixed process-regime Miocene clinothem sequence offshore New Jersey, USA. The quantitative, high-resolution grain-character data have enabled the topset, foreset, and bottomset deposits to be subdivided into three sedimentological packages, based on shared grain-character attributes. The topset core expression indicates that sedimentary packages M27–M29a and M27–M29c were deposited under a river-dominated process regime, as indicated by (1) widespread topset asymmetric ripple lamination; (2) terrestrial, woody organic matter; and (3) abundance of detrital quartz and glauconite sand grains. The topset core expression indicates that sedimentary package M27–M29b was

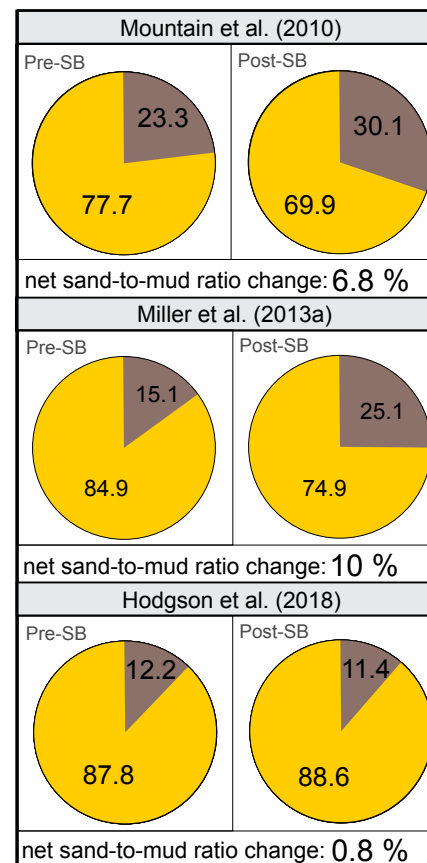


Figure 17. Pie charts showing average sand-to-mud composition by percentage volume across the candidate sequence boundaries (SB). The percentage difference in the sand:mud ratio was calculated using the values of the samples closest to the proposed sequence boundary (i.e., the closest sample below and above the candidate sequence boundary). For the Mountain et al. (2010) candidate sequence boundary, the samples are from 495.3 (below) and 494.8 (above) mcd. For the Miller et al. (2013a) candidate sequence boundary, the samples are from 512.97 (below) and 512.23 (above) mcd. For the Hodgson et al. (2018) candidate sequence boundary, the samples are from 519.8 (below) and 519.3 (above) mcd, where mcd—meters composite depth.

deposited under a wave- and storm-dominated process regime, as indicated by (1) widespread hummocky cross-stratification; (2) rhythmically laminated topset deposits; and (3) symmetrical ripple lamination.

The correlations of sedimentary packages across the topset-foreset-bottomset profile using high-resolution grain-character data provides a unique perspective into intraclinothem architecture and basin fill within a single seismic-scale clinothem. The dominant topset process regime exerts a fundamental control on the distribution of grain character. In this system, the sedimentary packages associated with river-dominated topset conditions have higher sand-to-mud ratios across the downdip profile; however, the grain character is texturally less-mature relative to the wave- and storm-dominated sedimentary package. The differences in grain character between the river-dominated and wave- and storm-dominated sedimentary packages are exaggerated downdip.

The sedimentary packages are separated by intraclinothem surfaces, which were determined objectively using changes in the average grain-size

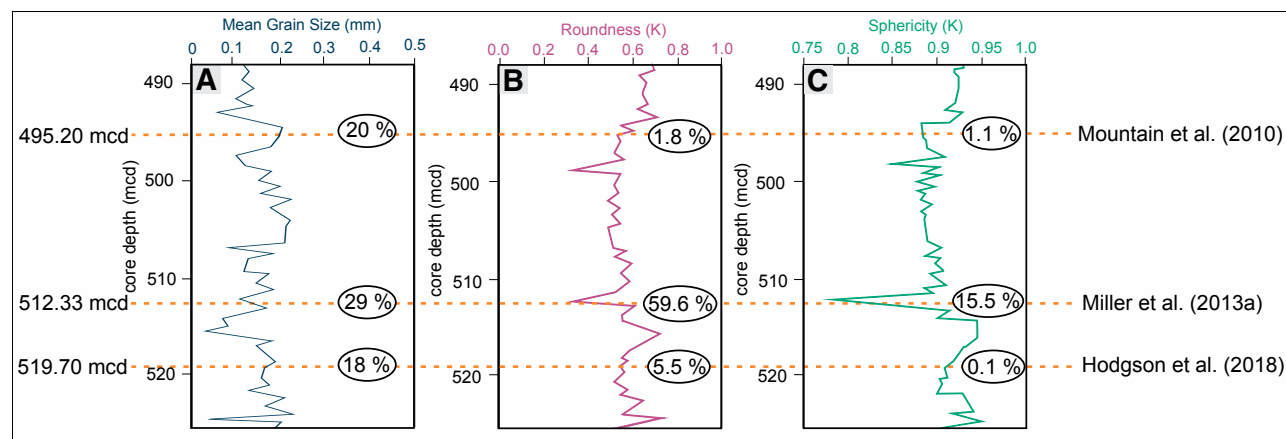


Figure 18. Percentage difference in grain character across candidate sequence boundaries: (A) mean grain size; (B) mean grain roundness; and (C) mean grain sphericity. The percentage differences were calculated using the values of the samples closest to the proposed sequence boundary (i.e., the closest sample below and above the candidate sequence boundary, where mcd—meters composite depth). See Figure 17 caption for sample positions.

distribution, and which are concomitant with stratigraphic changes in the facies, grain-size composition, and grain shape and sorting parameters. The identification of coeval sedimentary packages at subseismic resolution from grain character alone is a novel methodology for subdividing the stratigraphic record and provides a high-resolution correlation of strata within a sand-rich sequence. However, the data set does not resolve whether the intraclinothem surfaces are formed through autogenic or allogenic controls.

The high-resolution, quantitative grain-character data are also shown here to be an additional tool to help refine the placement of sequence boundaries. In this instance, the grain-character data were used to support the preferred placement of a sequence boundary position from three previously postulated candidate sequence boundaries. This was achieved by quantitatively assessing grain-size and grain shape change across the proposed sequence boundaries. Additionally, the new data presented here helped to refine and improve interpretations of stacking patterns and grain-size trends.

ACKNOWLEDGMENTS

We thank the Integrated Ocean Drilling Program (IODP), ECORD Science Operator (EOS), and the Bremen Core Repository (BCR) for assisting us with sample collection. We thank the Sorby Environmental Fluid Dynamics Laboratory (University of Leeds) for assistance with sample analysis. Finally, we thank an anonymous reviewer and reviewer C. Messina, Associate Editor A. Fildani, and Editor R. Russo for their constructive comments, which significantly improved the paper.

REFERENCES CITED

Adams, E.W., and Schlager, W., 2000, Basic types of submarine slope curvature: *Journal of Sedimentary Research*, v. 70, p. 814–828, <https://doi.org/10.1306/2DC4093A-0E47-11D7-8643000102C1865D>.

Ainsworth, R.B., Flint, S.S., and Howell, J.A., 2008, Predicting coastal depositional style: Influence of basin morphology and accommodation to sediment supply ratio within a sequence-stratigraphic framework, *in* Hampson, G.J., Steel, R.J., Burgess, P.M., and Dalrymple, R.W., eds., *Recent Advances in Models of Shallow-Marine Stratigraphy*: Society for Sedimentary Geology (SEPM) Special Publication 90, p. 237–263, <https://doi.org/10.2110/pec.08.90.0237>.

Ainsworth, R.B., Vakarelov, B.K., and Nanson, R.A., 2011, Dynamic spatial and temporal prediction of changes in depositional processes on clastic shorelines: Toward improved subsurface uncertainty reduction and management: *American Association of Petroleum Geologists Bulletin*, v. 95, p. 267–297, <https://doi.org/10.1306/06301010036>.

Armitage, J.J., Duller, R.A., Whittaker, A.C., and Allen, P.A., 2011, Transformation of tectonic and climatic signals from source to sedimentary archive: *Nature Geoscience*, v. 4, p. 231–235, <https://doi.org/10.1038/ngeo1087>.

Asquith, D.O., 1970, Depositional topography and major marine environments, Late Cretaceous, Wyoming: *American Association of Petroleum Geologists Bulletin*, v. 54, p. 1184–1224.

Barrett, B.J., Hodgson, D.M., Collier, R.E.L., and Dorrel, R.M., 2018, Novel 3D sequence stratigraphic numerical model for syn-rift basins: Analysing architectural responses to eustasy, sedimentation and tectonics: *Marine and Petroleum Geology*, v. 92, p. 270–284, <https://doi.org/10.1016/j.marpetgeo.2017.10.026>.

Bates, C.C., 1953, Rational theory of delta formation: *American Association of Petroleum Geologists Bulletin*, v. 37, p. 2119–2162.

Bhattacharya, J.P., 2006, Deltas, *in* Walker, R.G., and Posamentier, H., eds., *Facies Models Revisited*: Society for Sedimentary Geology (SEPM) Special Publication 84, p. 237–292, <https://doi.org/10.2110/pec.06.84.0237>.

Bhattacharya, J.P., and Giosan, L., 2003, Wave-influenced deltas: Geomorphological implications for facies reconstruction: *Sedimentology*, v. 50, p. 187–210, <https://doi.org/10.1046/j.1365-3091.2003.00545.x>.

Bhattacharya, J.P., and Walker, R.G., 1992, Deltas, *in* Walker, R.G., and James, N.P., eds., *Facies Models: Response to Sea Level Change*: St. Johns, Newfoundland, Geological Association of Canada, p. 157–177, <https://doi.org/10.1002/gj.3350290317>.

Blott, S.J., and Pye, K., 2001, GRADISTAT: A grain size distribution and statistics package for the analysis of unconsolidated sediments: *Earth Surface Processes and Landforms*, v. 26, p. 1237–1248, <https://doi.org/10.1002/esp.261>.

Browning, J.V., Miller, K.G., McLaughlin, P.P., Komins, M.A., Sugarman, P.J., Monteverde, D., Feigen-son, M.D., and Hernández, J.C., 2006, Quantification of the effects of eustasy, subsidence, and

- sediment supply on Miocene sequences, Mid-Atlantic margin of the United States: Geological Society of America Bulletin, v. 118, p. 567–588, <https://doi.org/10.1130/B25551.1>.
- Browning, J.V., Miller, K.G., Sugarman, P.J., Barron, J., McCarthy, F.M.G., Kulhanek, D.K., Katz, M.E., and Feigenson, M.D., 2013, Chronology of Eocene–Miocene sequences on the New Jersey shallow shelf: Implications for regional, interregional, and global correlations: *Geosphere*, v. 9, p. 1434–1456, <https://doi.org/10.1130/GES00857.1>.
- Bullimore, S., Henriksen, S., Liestøl, F.M., and Helland-Hansen, W., 2005, Clinoforms stacking patterns, shelf-edge trajectories and facies associations in Tertiary coastal deltas, offshore Norway: Implications for the prediction of lithology in prograding systems: *Norsk Geologisk Tidsskrift*, v. 85, p. 167–187, <https://doi.org/10.1111/j.1365-2117.2009.00432.x>.
- Burgess, P.M., and Hovius, N., 1998, Rates of delta progradation during highstands: Consequences for timing of deposition in deep-marine systems: *Journal of the Geological Society [London]*, v. 155, p. 217–222, <https://doi.org/10.1144/gsjgs.155.2.0217>.
- Carvajal, C., and Steel, R., 2006, Thick turbidite successions from supply-dominated shelves during sea-level highstand: *Geology*, v. 34, p. 665–668, <https://doi.org/10.1130/G22505.1>.
- Carvajal, C., and Steel, R., 2009, Shelf-edge architecture and bypass of sand to deep water: Influence of sediment supply, sea level, and shelf-edge processes: *Journal of Sedimentary Research*, v. 79, p. 652–672, <https://doi.org/10.2110/jsr.2009.074>.
- Carvajal, C., Steel, R., and Petter, A., 2009, Sediment supply: The main driver of shelf-margin growth: *Earth-Science Reviews*, v. 96, p. 221–248, <https://doi.org/10.1016/j.earscirev.2009.06.008>.
- Castelltort, S., and Van Den Driessche, G., 2003, How plausible are high-frequency sediment supply-driven cycles in the stratigraphic record?: *Sedimentary Geology*, v. 157, p. 3–13, [https://doi.org/10.1016/S0037-0738\(03\)00066-6](https://doi.org/10.1016/S0037-0738(03)00066-6).
- Catuneanu, O., Abreu, V., Bhattacharya, J.P., Blum, M.D., Dalrymple, R.W., Eriksson, P.G., Fielding, C.R., Fisher, W.L., Galloway, W.E., Gibling, M.R., Giles, K.A., Holbrook, K.A., Jordan, J.M., Kendall, R., Macurda, C.G. St., Macurda, C.B., Martinsen, O.J., Miall, A.D., Neal, J.E., Nummedal, D., Pomar, L., Posamentier, H.W., Pratt, B.R., Sarg, J.F., Shanley, K.W., Steel, R.J., Strasser, A., and Tucker, M.E.C., 2009, Towards the standardization of sequence stratigraphy: *Earth-Science Reviews*, v. 92, p. 1–33, <https://doi.org/10.1016/j.earscirev.2008.10.003>.
- Chen, S., Steel, R., Olariu, C., and Li, S., 2017, Growth of the paleo-Orinoco shelf margin prism: Process regimes, delta evolution, and sediment budget beyond the shelf edge: *Geological Society of America Bulletin*, v. 130, p. 35–63, <https://doi.org/10.1130/B31553.1>.
- Coleman, J.M., and Wright, L.D., 1975, Modern river deltas: Variability of processes and sand bodies, in Broussard, M.L., ed., *Deltas: Models for Exploration*: Houston, Texas, Houston Geological Society, p. 99–149.
- Cosgrove, G.I.E., Hodgson, D.M., Poyatos-Moré, M., Mountney, N.P., and McCaffrey, W.D., 2018, Filter or conveyor? Establishing relationships between clinoform rollover trajectory, sedimentary process regime, and grain character within intrashelf clinoforms, offshore New Jersey, USA: *Journal of Sedimentary Research*, v. 88, p. 917–941, <https://doi.org/10.2110/jsr.2018.44>.
- Deibert, J.E., Benda, T., Løseth, T., Schellpeper, M., and Steel, R.J., 2003, Eocene clinoform growth in front of a storm-wave-dominated shelf, Central Basin, Spitsbergen: No significant sand delivery to deepwater area: *Journal of Sedimentary Research*, v. 23, p. 546–558, <https://doi.org/10.1306/011703730546>.
- Dixon, J.F., Steel, R.J., and Olariu, C., 2012a, Shelf-edge delta regime as a predictor of the deep-water deposition: *Journal of Sedimentary Research*, v. 82, p. 681–687, <https://doi.org/10.2110/jsr.2012.59>.
- Dixon, J.F., Steel, R.J., and Olariu, C., 2012b, River-dominated shelf-edge deltas: Delivery of sand across the shelf break in the absence of slope incision: *Sedimentology*, v. 59, p. 1133–1157, <https://doi.org/10.1111/j.1365-3091.2011.01298.x>.
- Dott, R.J., and Bourgeois, J., 1982, Hummocky stratification: Significance of its variable bedding sequences: *Geological Society of America Bulletin*, v. 93, p. 663–680, [https://doi.org/10.1130/0016-7606\(1982\)93<663:HSSOIV>2.0.CO;2](https://doi.org/10.1130/0016-7606(1982)93<663:HSSOIV>2.0.CO;2).
- Fildani, A., Clark, J., Covault, J.A., Power, B., Romans, B.W., and Aiello, I.W., 2018, Muddy sand and sandy mud on the distal Mississippi Fan: Implications for lobe depositional processes: *Geosphere*, v. 14, p. 1051–1066, <https://doi.org/10.1130/GES01580.1>.
- Galloway, W.E., 1975, Process framework for describing the morphologic and stratigraphic evolution of deltaic depositional systems, in Broussard, M.L., ed., *Deltas: Models for Exploration*: Houston, Texas, Houston Geological Society, p. 87–98.
- Gilbert, G.K., 1885, The topographic feature of lake shores: U.S. Geological Survey Annual Report, v. 5, p. 104–108.
- Gomis-Cartesio, L.E., Poyatos-Moré, M., Flint, S.S., Hodgson, D.M., Brunt, R.L., and Wickens, H.D., 2017, Anatomy of a mixed-influence shelf edge delta, Karoo Basin, South Africa, in Hampson, G.J., Reynolds, A.D., Kostic, B., and Wells, M.R., eds., *Sedimentology of Paralic Reservoirs: Recent Advances*: Geological Society [London] Special Publication 444, p. 393–418, <https://doi.org/10.1144/SP444.5>.
- Grundvåg, S.A., Johannessen, E.P., Helland-Hansen, W., and Plink-Bjørklund, P., 2014, Depositional architecture and evolution of progradationally stacked lobe complexes in the Eocene Central Basin of Spitsbergen: *Sedimentology*, v. 61, p. 535–569, <https://doi.org/10.1111/sed.12067>.
- Hampson, G.J., 2016, Towards a sequence stratigraphic solution set for autogenic processes and allogenic controls: Upper Cretaceous strata, Book Cliffs, Utah, USA: *Journal of the Geological Society [London]*, v. 173, p. 817–836, <https://doi.org/10.1144/jgs2015-136>.
- Harms, J.C., Southard, J.B., and Walker, R.G., 1982, Structures and Sequences in Clastic Rocks: Society for Sedimentary Geology (SEPM) Short Course 9, 249 p., <https://doi.org/10.2110/scn.82.09>.
- Helland-Hansen, W., and Hampson, G.J., 2009, Trajectory analysis: Concepts and applications: *Basin Research*, v. 21, p. 454–483, <https://doi.org/10.1111/j.1365-2117.2009.00425.x>.
- Henriksen, S., Hampson, G.J., Helland-Hansen, W., Johannessen, E.P., and Steel, R.J., 2009, Shelf edge and shoreline trajectories, a dynamic approach to stratigraphic analysis: *Basin Research*, v. 21, p. 445–453, <https://doi.org/10.1111/j.1365-2117.2009.00432.x>.
- Hodgson, D.M., Kane, I.A., Flint, S.S., Brunt, R.L., and Ortiz-Karpf, A., 2016, Time-transgressive confinement on the slope and the progradation of basin-floor fans: Implications for the sequence stratigraphy of deep-water deposits: *Journal of Sedimentary Research*, v. 86, p. 73–86, <https://doi.org/10.2110/jsr.2016.3>.
- Hodgson, D.M., Browning, J.V., Miller, K.G., Hesselbo, S., Poyatos-Moré, M., Mountain, G.S., and Proust, J.-N., 2018, Sedimentology, stratigraphic context, and implications of Miocene bottomset deposits, offshore New Jersey, 2017: *Geosphere*, v. 14, p. 95–114, <https://doi.org/10.1130/GES01530.1>.
- Johannessen, E.P., and Steel, R.J., 2005, Shelf-margin clinoforms and prediction of deepwater sands: *Basin Research*, v. 17, p. 521–550, <https://doi.org/10.1111/j.1365-2117.2005.00278.x>.
- Jones, G.E.D., Hodgson, D.M., and Flint, S.S., 2015, Lateral variability in clinoform trajectory, process-regime, and sediment dispersal patterns beyond the shelf-edge rollover in exhumed basin margin-scale clinoforms: *Basin Research*, v. 27, p. 657–680, <https://doi.org/10.1111/bre.12092>.
- Katz, M.E., Browning, J.V., Miller, K.G., Monteverde, D.H., Mountain, G.S., and Williams, R.H., 2013, Paleobathymetry and sequence stratigraphic interpretations from benthic foraminifera: Insights on New Jersey shelf architecture, IODP Expedition 313: *Geosphere*, v. 9, p. 1488–1513, <https://doi.org/10.1130/GES00872.1>.
- Koo, W.M., Olariu, C., Steel, R.J., Olariu, M.I., Carvajal, C.R., and Kim, W., 2016, Coupling between shelf-edge architecture and submarine fan growth style in a supply-dominated margin: *Journal of Sedimentary Research*, v. 86, p. 613–628, <https://doi.org/10.2110/jsr.2016.42>.
- Li, Z., Bhattacharya, J.P. and Wang, J., 2011, Delta asymmetry: concepts, characteristics, and depositional models: *Petroleum Geoscience*, v. 8, p. 278–289, <https://doi.org/10.1007/s12182-011-0145-x>.
- McCubbin, D.G., 1982, Barrier-island and strand-plain facies, in Scholle, P.A., and Spearing, D., eds., *Sandstone Depositional Environments*: American Association of Petroleum Geologists Memoir 31 p. 247–279, [https://doi.org/10.1016/0037-0738\(92\)90037-R](https://doi.org/10.1016/0037-0738(92)90037-R).
- Mellere, D., Plink-Bjørklund, P., and Steel, R., 2002, Anatomy of shelf deltas at the edge of a prograding Eocene shelf margin, Spitsbergen: *Sedimentology*, v. 49, p. 1181–1206, <https://doi.org/10.1046/j.1365-3091.2002.00484.x>.
- Miller, K.G., and Snyder, S.W., eds., 1997, *Proceedings of the Ocean Drilling Program, Scientific Results Volume 150X*: College Station, Texas, Ocean Drilling Program, 374 p., <https://doi.org/10.2973/odp.proc.sr.150X.1997>.
- Miller, K.G., Browning, J.V., Mountain, G.S., Bassetti, M.A., Monteverde, D., Katz, M.E., Inwood, J., Lofi, J., and Proust, J.-N., 2013a, Sequence boundaries are impedance contrasts: Core-seismic-log integration of Oligocene–Miocene sequences, New Jersey shallow shelf: *Geosphere*, v. 9, p. 1257–1285, <https://doi.org/10.1130/GES00858.1>.
- Miller, K.G., Mountain, G.S., Browning, J.V., Katz, M.E., Monteverde, D.H., Sugarman, P.J., Ando, H., Bassetti, M.A., Bjerrum, C.J., Hodgson, D., Hesselbo, S., Karakaya, S., Proust, J.-N., and Rabineau, M., 2013b, Testing sequence stratigraphic models by drilling Miocene foresets on the New Jersey shallow shelf: *Geosphere*, v. 9, p. 1236–1256, <https://doi.org/10.1130/GES00884.1>.
- Miller, K.G., Lombardi, C.J., Browning, J.V., Schmelz, W.J., Gallegos, G., Mountain, G.S., Baldwin, K.E., 2018, Back to basics of sequence stratigraphy, Early Miocene and Mid-Cretaceous examples from the New Jersey palaeoshelf: *Journal of Sedimentary Research*, v. 88, p. 148–176, <https://doi.org/10.2110/jsr.2017.73>.
- Mitchum, R.M., Vail, P.R., and Thompson, S., 1977, Seismic stratigraphy and global changes in sea level: Part 2. The depositional sequence as the basic unit for stratigraphic analysis, in

- Payton, C.E., ed., *Seismic Stratigraphy: Applications to Hydrocarbon Exploration: American Association of Petroleum Geologists Memoir 26*, p. 53–62.
- Monteverde, D.H., Mountain, G.S., and Miller, K.G., 2008, Early Miocene sequence development across the New Jersey margin: *Basin Research*, v. 20, p. 249–267, <https://doi.org/10.1111/j.1365-2117.2008.00351.x>.
- Moore, A., Goff, J., McAdoo, B.G., Fritz, H.M., Gusman, A., Kalligeris, N., Kalsum, K., Susanto, A., Suteja, D., and Synolakis, C.E., 2011, Sedimentary deposits from the 17 July 2006 western Java tsunami, Indonesia: Use of grain size analyses to assess tsunami flow depth, speed, and traction carpet characteristics: *Pure and Applied Geophysics*, v. 168, p. 1951–1961, <https://doi.org/10.1007/s00024-011-0280-8>.
- Mountain, G.S., Proust, J.-N., McInroy, D., and Cotterill, C., and the Expedition 313 Scientists, 2010, Initial Report: Proceedings of the International Ocean Drilling Program, Expedition 313: College Station, Texas, International Ocean Drilling Program, 885 p., <https://doi.org/10.2204/iodp.proc.313.101.2010>.
- Mulder, T., and Alexander, J., 2001, The physical character of subaqueous sedimentary density flows and their deposits: *Sedimentology*, v. 48, p. 269–299, <https://doi.org/10.1046/j.1365-3091.2001.00360.x>.
- Muto, T., and Steel, R.J., 2002, Role of autoretreat and A/S changes in the understanding of deltaic shoreline trajectory: A semi-quantitative approach: *Basin Research*, v. 14, p. 303–318, <https://doi.org/10.1046/j.1365-2117.2002.00179.x>.
- Normark, W.R., and Piper, D.J., 1991, Initiation processes and flow evolution of turbidity currents: Implications for the depositional record, in Osborne, R.H., ed., *From Shoreline to Abyss: Contributions to Marine Geology in Honor of Francis Parker Shepard*: Society for Sedimentary Geology (SEPM) Special Publication 46, p. 207–230.
- Olariu, C., 2014, Autogenic process change in modern deltas: Lessons from the ancient, in Martinus, A.W., Ravnås, R., Howell, J.A., Steel, R.J., and Wonham, J.P., eds., *From Depositional Systems to Sedimentary Successions on the Norwegian Continental Margin*: International Association of Sedimentologists, Special Publication 46, p. 149–166, <https://doi.org/10.1002/9781118920435.ch7>.
- Patruno, S., Hampson, G.J., and Jackson, C.A.-L., 2015, Quantitative characterisation of deltaic and subaqueous clinoforms: *Earth-Science Reviews*, v. 142, p. 79–119, <https://doi.org/10.1016/j.earscirev.2015.01.004>.
- Pellegrini, C., Maselli, V., Gamberi, F., Asioli, A., Bohacs, K.M., Drexler, T.M., and Trincardi, F., 2017, How to make a 350-m-thick lowstand systems tract in 17,000 years: The late Pleistocene Po River (Italy) lowstand wedge: *Geological Society of America Bulletin*, v. 45, p. 327–330, <https://doi.org/10.1130/G38848.1>.
- Pirmez, C., Pratson, L.F., and Steckler, M.S., 1998, Clinoform development by advection–diffusion of suspended sediment: Modelling and comparison to natural systems: *Journal of Geophysical Research*, v. 103, p. 24,141–24,157, <https://doi.org/10.1029/98JB01516>.
- Plink-Björklund, P., and Steel, R.J., 2004, Initiation of turbidity currents: Outcrop evidence for Eocene hyperpycnal-flow turbidites: *Sedimentary Geology*, v. 165, p. 29–52, <https://doi.org/10.1016/j.sedgeo.2003.10.013>.
- Poag, C.W., 1985, Depositional history and stratigraphic reference section for central Baltimore Canyon trough, in Poag, C.W., ed., *Geologic Evolution of the United States Atlantic Margin*: New York, Van Nostrand Reinhold, p. 217–264.
- Poag, C.W., and Sevon, W.D., 1989, A record of Appalachian denudation in postrift Mesozoic and Cenozoic sedimentary deposits of the U.S. middle Atlantic continental margin: *Geomorphology*, v. 2, p. 119–157, [https://doi.org/10.1016/0169-555X\(89\)90009-3](https://doi.org/10.1016/0169-555X(89)90009-3).
- Prélat, A., Pankhania, S.S., Jackson, C.A.-L., and Hodgson, D.M., 2015, Slope gradient and lithology as controls on the initiation of submarine slope gullies: Insights from the North Carnarvon Basin, offshore NW Australia: *Sedimentary Geology*, v. 329, p. 12–17, <https://doi.org/10.1016/j.sedgeo.2015.08.009>.
- Proust, J.N., Poudroux, H., Ando, H., Hesselbo, S.P., Hodgson, D.M., Lofi, J., Rabineau, M., and Sugarman, P.J., 2018, Facies architecture of Miocene subaqueous clinofolds of the New Jersey passive margin: Results from IODP-ICDP Expedition 313: *Geosphere*, v. 14, p. 1564–1591, <https://doi.org/10.1130/GES01545.1>.
- Reineck, H.E., and Singh, I.B., 1972, Genesis of laminated sand and graded rhythmites in storm-sand layers of shelf mud: *Sedimentology*, v. 18, p. 123–128, <https://doi.org/10.1111/j.1365-3091.1972.tb00007.x>.
- Reynolds, D.J., Steckler, M.S., and Coakley, B.J., 1991, The role of the sediment load in sequence stratigraphy: The influence of flexural isostasy and compaction: *Journal of Geophysical Research—Solid Earth*, v. 96, p. 6931–6949, <https://doi.org/10.1029/90JB01914>.
- Rich, J.L., 1951, Three critical environments of deposition and criteria for recognition of rocks deposited in each of them: *Geological Society of America Bulletin*, v. 62, p. 1–20, [https://doi.org/10.1130/0016-7606\(1951\)62\[1:TCEODA\]2.0.CO;2](https://doi.org/10.1130/0016-7606(1951)62[1:TCEODA]2.0.CO;2).
- Rossi, V.M., and Steel, R.J., 2016, The role of tidal, wave and river currents in the evolution of mixed-energy deltas: Example from the Lajas Formation (Argentina): *Sedimentology*, v. 63, p. 824–864, <https://doi.org/10.1111/sed.12240>.
- Ryan, M., Helland-Hansen, W., Johannessen, E.P., and Steel, R.J., 2009, Erosional vs accretionary shelf margins: The influence of margin type on deepwater sedimentation—An example from the Porcupine Basin, offshore western Ireland, in Henriksen, S., Hampson, G.J., Helland-Hansen, W., Johannessen, E.P., and Steel, R.J., eds., *Trajectory Analysis in Stratigraphy: Basin Research*, v. 21, p. 676–703, <https://doi.org/10.1111/j.1365-2117.2009.00424.x>.
- Sheridan, R.E., and Grow, J.A., 1988, U.S. Atlantic continental margin: A typical Atlantic-type or passive continental margin, in Sheridan, R.E., and Grow, J.A., eds., *The Atlantic Continental Margin, U.S.: Boulder, Colorado, Geological Society of America, The Geology of North America*, v. I-2, p. 1–7, <https://doi.org/10.1130/DNAG-GNA-12>.
- Steel, R.J., and Olsen, T., 2002, Clinoforms, clinoform trajectory and deepwater sands, in Armentrout, J.M., and Rosen, N.C., eds., *Sequence Stratigraphic Models for Exploration and Production: Evolving Methodology, Emerging Models and Application Histories: Proceeding of the 22nd Annual Bob F. Perkins Research Conference, Gulf Coast Section (Dallas, Texas): Society of Economic Paleontologists and Mineralogists (GCS-SEPM)*, p. 367–381, <https://doi.org/10.5724/gcs.02.22.0367>.
- Stevenson, C., Jackson C.A.-L., Hodgson, D.M., Hubbard, S.M., and Eggenhuisen, J.T., 2015, Deep-water sediment bypass: *Journal of Sedimentary Research*, v. 87, p. 1058–1081, <https://doi.org/10.2110/jsr.2015.63>.
- Sugarman, P.J., Miller, K.G., Owens, J.P., and Feigenson, M.D., 1993, Strontium-isotope and sequence stratigraphy of the Miocene Kirkwood Formation, southern New Jersey: *Geological Society of America Bulletin*, v. 105, p. 423–436, [https://doi.org/10.1130/0016-7606\(1993\)105<0423:SIASSO>2.3.CO;2](https://doi.org/10.1130/0016-7606(1993)105<0423:SIASSO>2.3.CO;2).
- Ta, T.K.O., Nguyen, V.L., Tateishi, M., Kobayashi, I., Saito, Y., and Nakamura, T., 2002, Sediment facies and late Holocene progradation of the Mekong River Delta in Bentre Province, southern Vietnam: An example of evolution from a tide-dominated to a tide- and wave-dominated delta: *Sedimentary Geology*, v. 152, p. 313–325, [https://doi.org/10.1016/S0037-0738\(02\)00098-2](https://doi.org/10.1016/S0037-0738(02)00098-2).
- Udden, J.A., 1914, Mechanical composition of clastic sediments: *Geological Society of America Bulletin*, v. 25, p. 655–744, <https://doi.org/10.1130/GSAB-25-655>.
- Uroza, C.A., and Steel, R.J., 2008, A highstand shelf-margin delta system from the Eocene of West Spitsbergen, Norway: *Sedimentary Geology*, v. 203, p. 229–245, <https://doi.org/10.1016/j.sedgeo.2007.12.003>.
- Watts, A.B., and Steckler, M.S., 1979, Subsidence and eustasy at the continental margin of eastern North America, in Talwani, M., Hay, W., and Ryan, W.B.F., eds., *Deep Drilling Results in the Atlantic Ocean: Continental Margins and Paleoenvironment*: Washington, D.C., American Geophysical Union, Maurice Ewing Series Volume 3, p. 218–234, <https://doi.org/10.1029/ME003p0218>.
- Wentworth, C.K., 1922, A scale of grade and class terms for clastic sediments: *The Journal of Geology*, v. 30, p. 377–392, <https://doi.org/10.1086/622910>.
- Wild, R., Flint, S.S., and Hodgson, D.M., 2009, Stratigraphic evolution of the upper slope and shelf edge in the Karoo Basin, South Africa: *Basin Research*, v. 21, p. 502–527, <https://doi.org/10.1111/j.1365-2117.2009.00409.x>.
- Withjack, M.O., Schlische, R.W., and Olsen, P.E., 1998, Diachronous rifting, drifting, and inversion on the passive margin of eastern North America: An analogue for other passive margins: *American Association of Petroleum Geologists Bulletin*, v. 82, p. 817–835, <https://doi.org/10.1306/1D9BC60B-172D-11D7-8645000102C1865D>.
- Zavala, C., Gamero, H., and Arcuri, M., 2006, Lifting rhythmites: A diagnostic feature for the recognition of hyperpycnal deposits [abs.]: *Geological Society of America Abstracts with Programs*, v. 38, no. 7, p. 541.